Marine Geophysical Research (2020) 41:20
https://doi.org/10.1007/s11001-020-09419-5

ORIGINAL RESEARCH PAPER

Uppermost crustal structure across the eastern Lau spreading center from P-to-S converted waves

Charu Lata[1] · **Robert A. Dunn**[1]

Received: 21 March 2020 / Accepted: 12 October 2020

Abstract

P and S wave data from the L-SCAN active-source wide-angle reflection/refraction experiment are modelled to investigate upper crustal structure in the Lau backarc basin. A combination of ray tracing and finite difference numerical wavefield simulation is used to identify P and P-to-S converted seismic phases. The phases primarily arise from two shallow interfaces, one at ~ 80 m depth or less, and the other at 500–650 m depth. The shallower interface is deeper than the sediment base, is observed across the study area, and is interpreted as a 'layer 2Aa' boundary, proposed to result from a rapid change in crack density. The deeper interface is interpreted as the layer 2A–2B boundary, corresponding to a transition from lavas to sheeted dykes. Layer 2A, on average, is 150 m thicker in crust that formed at the spreading center when spreading was located near the arc (< 50 km away), as compared to when spreading was located farther away from the arc (> 70 km away). Layer 2A thickness and *Vp*/*Vs* values indicate that a thicker and more porous lava layer, dominated by basalts to basalt-andesites, cap near-arc crust, while a thinner and less-porous, mostly basaltic, volcanic layer caps the far-arc crust. These results are consistent with the waning influence of slab-derived volatiles on crustal formation as seafloor spreading moves away from the active arc.

Keywords Oceanic crust · S-waves · Backarc spreading center · Subduction zone

Introduction

Along mid-ocean ridges, spreading rate is a dominant factor that controls crustal formation and structure (Reid and Jackson, 1981; Parmentier and Morgan, 1990). In contrast, along oceanic back-arc spreading centers, slab-derived volatiles, principally water, appear to influence melting processes and crustal formation, overprinting spreading-rate trends (Martinez and Taylor, 2002; Eason and Dunn, 2015). The presence of water during melting is expected to enhance melt production (e.g. Davies and Bickle, 1991; Stolper and Newman, 1994), with the water ending up in the melt (e.g. Hirth and Kohlstedt, 1996), and may lead to more silicic lavas (e.g. Sisson and Grove, 1992; Gaetani and Grove, 1994; Eason and Dunn, 2015). A principle observation is that when a back-arc spreading ridge is located close to an active arc system, the magma supply to the ridge appears to be relatively high, with a corresponding thicker upper-crustal extrusive layer and a greater total crustal thickness (Martinez and Taylor 2002; Dunn and Martinez 2011; Arai and Dunn 2014). In addition, lavas erupted at the ridge have higher water contents, with compositions ranging from basalts, to andesites, to rhyolites (e.g. Jenner et al. 1987; Tamura et al. 2008).

Along the active Eastern Lau Spreading Center (ELSC) in the Lau back-arc basin, studies have revealed systematic variations in crustal structure formed at the spreading center as a function of distance to the volcanic arc. For example, as the axis of the spreading center approaches the arc to the south, seismic layer 2A (a proxy for the extrusive layer) is observed to thicken, while the average P-wave velocity of layer 2A decreases (Jacobs et al. 2007), an indication of greater porosity and more silicic lavas. More generally across the Lau basin, crust formed near the Tofua Arc is abnormally thick (8–9 km) and compositionally stratified, with a thick low-velocity upper crust and an abnormally

Electronic supplementary material The online version of this article (https://doi.org/10.1007/s11001-020-09419-5) contains supplementary material, which is available to authorized users.

✉ Charu Lata
charu.iitkgp@gmail.com

[1] Department of Earth Sciences, University of Hawai'i-Mānoa, 1680 East-West Road, Honolulu, HI 96822, USA

Published online: 02 November 2020

high-velocity lower crust (Arai and Dunn, 2014). Lava samples from these areas have arc-like compositional enrichments and tend to be more vesicular and differentiated than typical mid-ocean ridge basalts (Pearce et al. 1994; Escrig et al. 2009). Eason and Dunn (2015) propose that slab-derived water entrained in the near-arc ridge system not only enhances mantle melting, but also affects magmatic differentiation and crustal accretion processes.

With a rough association between seismic layer 2A and extrusive basalts, we mapped out variations in layer 2A thickness and wave speed to better understand variations across these crustal domains with respect to extrusive layer properties. Upper crustal interfaces such as the base of a sediment layer and base of layer 2A are strong first order seismic discontinuities that can cause compressional seismic phases (P waves) to convert to shear phases (S waves) (e.g. White and Stephen, 1980; Christeson et al. 1997; Eccles et al. 2009). Such phase converted arrivals were strongly and consistently recorded on 3-component ocean-bottom seismographs located across the Lau basin during the L-SCAN active-source seismic experiment (Dunn et al. 2013). We examine the phase converted arrivals here to reveal details of crustal structure and formation.

Study area

The Eastern Lau Spreading Center (ELSC) is located within the Lau Basin (Fig. 1a inset), which is a wedge-shaped back-arc basin bordered by the Lau Ridge remnant arc to the west and the currently active Tofua arc to the east (Karig 1970; Hawkins 1995). The basin is proposed to have opened ~ 6 My ago (Hawkins 1994) as a result of arc rifting and crustal extension. The basin opening was accommodated by regions of localized seafloor spreading, along with more diffuse spreading and magmatic intrusion, giving rise to an uneven and discontinuous seafloor (Taylor et al. 1996; Austin 2012). Between 2 and 4 My, crustal extension was dominated by the southward propagation of seafloor spreading (Parson et al. 1990; Hawkins 1994; Taylor et al. 1996), which continues today along the Central Lau Spreading Center (CLSC), ELSC and Valu Fa Ridge (VFR). Along these spreading centers, the spreading rate decreases from north to south: from ~ 90 mm/year in the north at the CLSC, to ~ 60 mm/year at the southern ELSC, to ~ 40 mm/year at the VFR (Taylor et al. 1996; Zellmer and Taylor 2001).

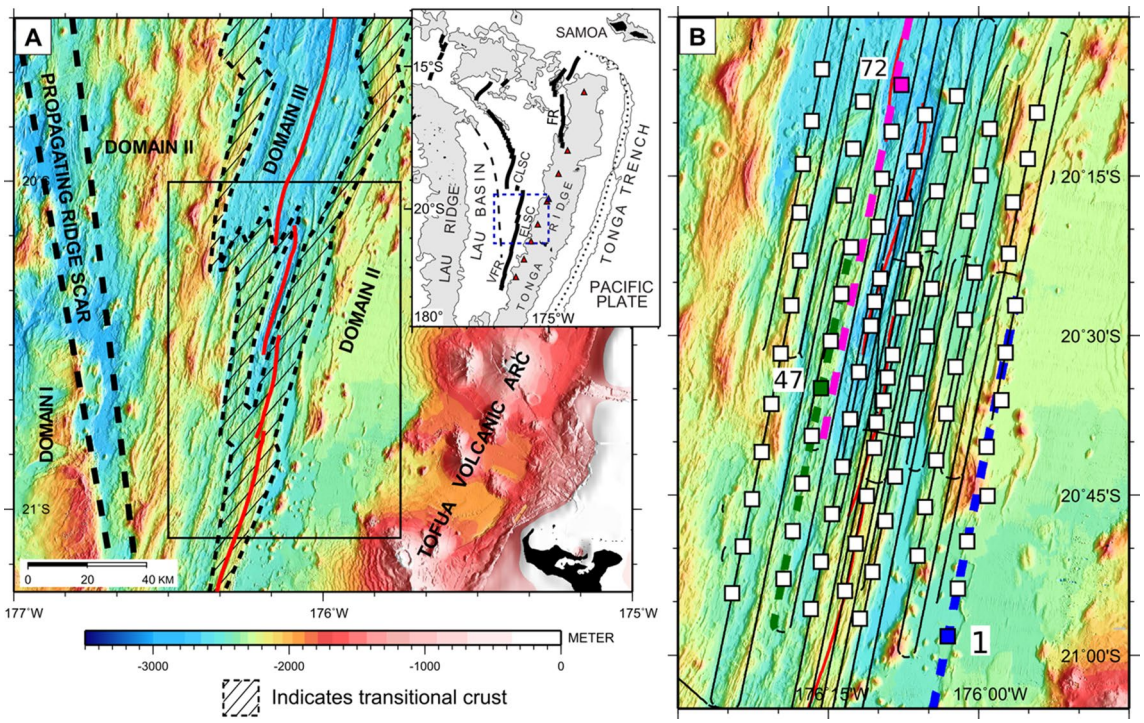

Fig. 1 Bathymetry map of the study area and layout of the L-SCAN experiment. Panel (**a**) shows a bathymetry map overlain by dashed lines and labels to indicate the crustal domains, as described in "Crustal domains" sect. The inset shows the overall location of the study area. The black box indicates the area shown in **b**. Panel (**b**) shows locations of ocean bottom seismographs (squares) and the subset of seismic source lines (black lines) used in this study. The colored OBS and colored dashed lines (shown in blue, magenta, and green) refer to sources and source lines discussed in "Observations" sect. and shown in Figs. 3 and 4. Figure modified from Dunn et al. (2013)

Crustal domains

Along mid-ocean ridges, as the spreading rate decreases the melt flux due to passive upwelling decreases, and the ridge axis is expected to transform from an axial high, bounded by faults with relatively small throws, to an axial valley, bounded by faults with large throws (e.g. Small and Sandwell 1989; Lin and Morgan 1992; Morgan and Chen 1993a, b). However, along the ELSC opposite trends are observed. From north to south, as the spreading rate decreases the distance between the axis of the ELSC and the active Tofua Arc decreases by ~ 40 km. As this happens, the ridge morphology changes from a more faulted and deep rifted valley to a less faulted and broad axial high. Furthermore, lava samples from the ridge axis show stronger enrichments in subduction-related components relative to mid-ocean ridge basalts in the south (Escrig et al. 2009). In addition, lava samples from the southern ELSC are more evolved (basaltic andesites) and highly vesicular as compared to the northern ELSC (e.g. Jenner et al. 1987; Vallier et al. 1991; Pearce et al. 1994). Since this discovery, several studies have investigated the anomalous nature of crust formed along the ridge axis. Martinez and Taylor (2002) identified large domains across the Lau basin composed of differences in bathymetry and seafloor morphology, Bouguer gravity, rock chemistry, and other properties. They proposed that arc proximity overrides spreading rate controls on crustal formation.

More recent seismic studies have also found corresponding changes in internal crustal structure as a function of arc proximity (Dunn and Martinez 2011; Dunn et al. 2013; Arai and Dunn 2014). Basin crust that was produced when the ridge was close to the arc is thicker and unusually stratified, with a thick low-velocity (3.4–4.5 km/s) upper crust and an abnormally high-velocity (7.2–7.4 + km/s) lower crust (Dunn et al. 2013; Arai and Dunn 2014). Due to symmetric spreading, the ridge axis has produced this type of crust on both sides of the spreading center, leading to large semi-symmetric domains of anomalous crustal properties across the basin (Domain II in Fig. 1a; Domain I is the crust produced in the basin before the ELSC propagated southward into its present location). On the other hand, crust produced when the ridge was farther away from the arc is less anomalous, and has a similar thickness and velocity structure as that formed at intermediate-spreading rate mid-ocean ridges (Domain III in Fig. 1a).

The general consensus of these and other studies is that the change from anomalous crust to more typical crust is controlled by the waning influence of slab-derived volatiles on the magma supply as the distance between ridge and arc increases. The mechanism of this influence, and processes that generate the unusual crustal stratification, was further studied by Eason and Dunn (2015). They proposed that slab-derived water entrained in the near-arc ridge system not only enhances mantle melting and crustal thickness, as commonly proposed to explain high crustal production in back-arc environments, but also affects magmatic differentiation and crustal accretion processes leading to the observed differences in lava composition and vertical crustal structure. In their model, slab-derived water in melts suppresses plagioclase crystallization and leads to the formation of an ultramafic lower crust, with higher seismic velocities, and a more felsic upper crust with unusually low seismic velocities, while successfully predicting major element compositional trends of the erupted lavas.

Upper oceanic crustal layer 2A

Oceanic crust formed along intermediate-to-fast spreading-rate ridges is often considered to have, on average, a simple vertical structure. From the top, the sequence first consists of a shallow crustal layer of a few hundred meters thickness characterized by low seismic velocities (< 5 km/s P-wave velocity) and high seismic attenuation, the lower boundary of which is marked by a strong velocity gradient that can be imaged with seismic reflection techniques (e.g. Harding et al. 1993; Vera and Diebold 1994; Wilcock et al. 1995; Detrick et al. 1998). Known as seismic layer 2A, it is often interpreted in terms of a lithology composed of high-porosity extrusive basalts, based on analogy with ophiolite units (subaerial exposures of oceanic and back-arc crust) (e.g. Coleman 1977; Nicolas 1989; Dilek and Furnes 2011), the seismic velocity of laboratory samples of dredged and drilled rocks, in situ measurements in drill holes (e.g. Detrick et al. 1994; Karson 1998), and observations within "tectonic windows" into oceanic crust, such as Hess Deep (Karson et al., 2002). By further analogy to ophiolites and other observations, seismic layer 2A is underlain by a higher-velocity region, with a lower seismic gradient, of sheeted dikes (seismic layer 2B; 4.5–6 km/s P-wave velocity), followed by an even higher-velocity region of gabbro composition (layer 3; 6.5–7 km/s P-wave velocity). These three layers together form the crustal assembly, which is generally 6–7 km thick (White et al. 1992). This simple model has served for many years to provide a framework for broader investigation and comparisons, but it is now known that ocean crust varies strongly from setting to setting, and does not always conform to these expectations (e.g. Livermore et al. 1997; Martinez and Taylor 2002; Becker et al. 2010).

A few seismic studies have investigated the structure of seismic layer 2A along and across the ELSC. The most significant was published by Jacobs et al. (2007), which showed systematic variations in seismic layer 2A thickness and interval velocities along the ridge crest as a function of distance to the volcanic arc. Along the ELSC within our study area, the average thickness of layer 2A increases from 0.5 to 0.62 km from north to south, while the average P-wave speed

in layer 2A decreases from 3 km/s to 2.68 km/s, correlating with the change in lava composition from basalt to basaltic-andesite and with increased porosity. Results from this study, however, were limited to source lines located strictly along the axis of the spreading center.

A second seismic study was the L-SCAN active-source seismic tomography experiment (Dunn and Martinez 2011; Dunn et al. 2013; Arai and Dunn 2014; Dunn 2015), which spanned crustal Domains II and III, and the narrow transition zone between them. Although the smooth tomography models prevent the identification of the base of layer 2A within acceptable limits for this study, the tomographic images show detailed lateral variations of seismic structure in the upper crustal layers extending well away from the ridge. In particular, the upper 1 km of crust exhibits prominent domain-specific lateral variations in velocities, with average P-wave velocity of ~ 4 km/s in Domain II as compared to 5 km/s in Domain III. Furthermore, along the direction of spreading (perpendicular to the ridge axis) crustal domains exhibit step-like transitions in properties with as little as 5 km of incremental spreading, matching observed changes in seafloor depth and Bouguer gravity structure (Martinez and Taylor 2002).

Experiment layout and data processing

The L-SCAN seismic experiment (Dunn et al. 2013) consisted of 83 ocean bottom seismographs (OBS), each containing a hydrophone and a gimballed 3-component geophone, placed on the seafloor in a grid formation. The seismic source was the R/V Langseth's 36-element, 6600 in^3 airgun array towed at 9 m depth with sources located every 450–500 m. Fifty-seven dense source lines were carried out such that most OBSs were crossed by at least a ridge-perpendicular and a ridge-parallel pair of lines. See Dunn et al. (2013) for further details.

In this study, data processing steps included removing the instrument response from each channel, rotation of data components to increase the relative amplitudes of P-waves and S-wave in two principal directions with respect to each shot, frequency filtering, and a small amount of amplitude correction to adjust for geometric and intrinsic attenuation with increasing shot-to-receiver range. Because the in situ orientation of the horizontal components of the sensor was not known, water wave polarisation analysis was used to estimate them. The direct water wave first breaks were picked on record sections of the hydrophone channel, and then a 0.1 s time window after each pick was used to extract particle motions on the geophone channels. The geophone horizontal component orientation was then calculated by maximizing the radial energy as compared to the transverse energy, while maintaining positive polarity of the water wave on the radial component (e.g. Bratt and Solomon 1984; Anderson et al. 1987). Given the density of source lines around any one station, nearly complete azimuthal coverage for most stations was available, and orientation uncertainties were $\leq 5^0$. Out of 83 instruments, 50 were selected for this study (Fig. 1b). The remaining instruments were discarded due to one or more inoperative components, component gain issues, poor signal-to-noise ratio, and/or intermittent ~ 6 Hz instrument noise issues. A complete listing is given in Online Resource 1.

Since wide-angle crustal P-wave refractions that arrive at non-vertical angles below the seafloor appear on radial records, this energy was minimised by performing another component rotation about the transverse axis to rotate Z-R components to L-Q components (Fig. 2b). This was done to increase the relative amplitude of P waves on the L component and S waves on the Q component (a description is given in Online Resource 2), mainly for far-offset data. However, due to scattering, dipping layers, and other non-2-D effects, the isolation of the P and vertically-polarized S waves (SV) is approximate. In the following analysis, only ridge-parallel source lines were used to avoid directional effects on wave speed and travel time, since the upper 1 km of crust exhibits ~ 3% P-wave anisotropy with the fast axis oriented parallel the ridge (Dunn 2015).

Observations

In an oceanic environment, P-to-S wave conversions can occur at sharp structural boundaries such as the seafloor and upper crustal layers, either along the downgoing ray path or the upgoing path beneath the receiver. Figure 2 schematically depicts example phase conversions, which are just a few of several possibilities. Those shown, as discussed below, are dominant in seismic record sections in this environment. S waves can be identified by their unique orientations and slower travel times than P waves. However, the S waves may be coincident in time with P wave multiples, especially reverberations in the upper crustal or sediment layers, and because the P and P-to-S converted waves may have differing ray parameters, the S wave may appear on data records rotated to show P waves alone. Therefore, further distinguishing characteristics of S waves are required, such as their traveltime moveout and amplitude variation with range.

Several phase converted arrivals were identified in data recorded across the entire compliment of the 50 receivers. Figure 3 shows examples of common-receiver-gather record sections, to 10 km range, for three receivers located within the different crustal domains (Z and R data components). The source lines and receiver locations are shown in Fig. 1b. Within 2 km range, the first waves to arrive are water waves; their arrival times at all ranges are marked in blue. At ranges

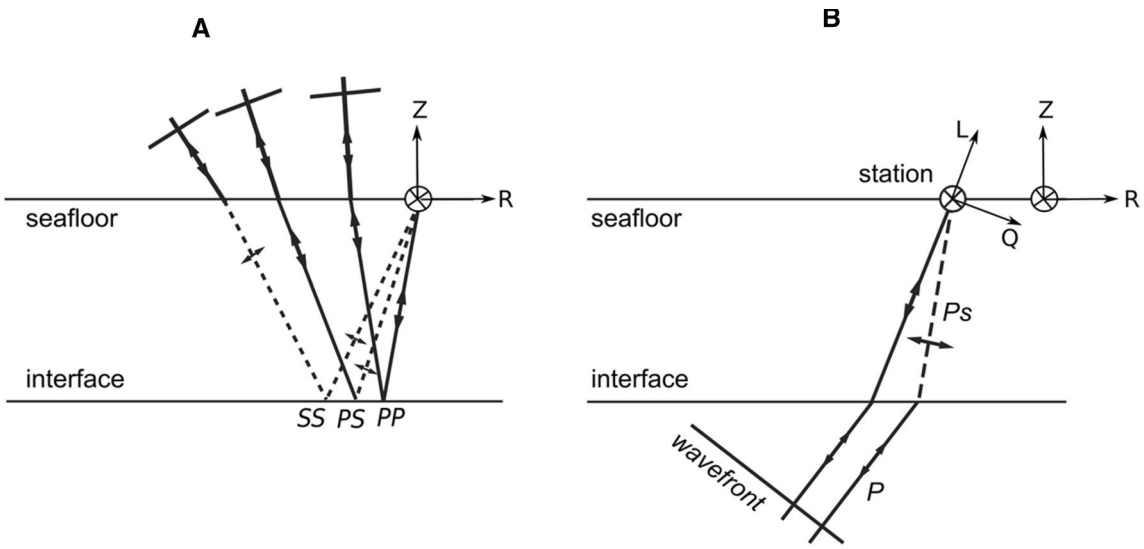

Fig. 2 Schematic ray diagram showing wave phase conversion. **a** A water wave incident on the seafloor with phase conversions at the seafloor and at a reflecting interface below the station are shown. PP is transmitted at the seafloor and reflected at the interface as a P-wave, PS is transmitted as a P-wave and reflected as a S-wave, and SS is transmitted and reflected as a S-wave. **b** An upgoing refracted P-wave below the station is shown, along with a P-to-S conversion at an interface below the station, called a Ps wave. The orientation of rotated instrument components, about the transverse axis, is also shown

greater than a few hundred meters, the water wave appears on both the vertical and radial components due to oblique arrival at the seafloor. Behind the water wave arrival, at larger travel times, additional arrivals are clearly observed at stations 47 and 1, located 11 km and 20 km from the ridge crest (in the transition zone and Domain II), respectively. These nearly 'water-wave parallel' arrivals could be reflected PP, PS, or SS converted waves from the base of a sediment or upper crustal layer (Fig. 2a), or multiples within layers. "Methods and Preliminary Results" describes how the different phases were identified and modelled.

At shot ranges of ~ 2–30 km, seismic phases travelling through the crust arrive before the water wave. Figure 4, shows these deeper arrivals for the same stations in Fig. 3. Here L and Q component records are plotted rather than Z and R (as in Fig. 3) to isolate the P and S arrivals. These include crustal P-wave refractions from layers 2 and 3 that appear strongly on the L component. Layer 2 P-wave refractions are detected at 2–10 km range, with apparent speeds of 4–5 km/s and arrive at the station with estimated incidence angles between 10º and 15º (on the basis of wave polarizations). Layer 3 P-wave refractions are detected at 8–30 km range with apparent speeds of 6.8–7.4 km/s and arrive at the station with estimated incidence angles of less than 10º. The P-to-S converted waves (Ps) closely follow the crustal P refraction and are recorded on the Q component. The Ps arrivals have similar apparent velocities as the pre-arriving P phase, which indicates that the P-to-S conversion occurs beneath the receiver (Fig. 2b). This conversion could occur at the strong upper crustal seismic discontinuities such as the sediment base, or deeper at a layer 2A-2B boundary within the igneous crust. Also arriving behind the Ps phase and closely following the Ps or P traveltime curve, are shear wave reverberated arrivals. These reverberations occur within the upper crustal layers, due to their near-parallel nature of traveltimes with respect to the P or Ps phase. The Ps and its multiples were not consistently observed on both sides of the receiver, possibly indicating source side scattering effects or local variations in structure beneath a receiver.

The mean traveltime difference between the P and Ps phases at each station is observed to spatially vary across the crustal domains (Fig. 4). For example, the receiver at station 72, located in Domain III and 2 km away from the ridge axis, exhibits a Ps versus P traveltime difference of ~ 0.15 s. While the receiver at station 47, located in the transition zone and 11 km from the ridge axis, recorded a delay of ~ 0.6 s. The greatest difference, ~ 0.8 s, was observed at station 1, located in Domain II and 20 km away from the ridge axis. Overall, the traveltime delays correlate positively with the distance of a receiver from the ridge axis. Since, in general, sediment thickness correlates positively with distance from the ridge axis, one possibility is that the observed S-wave arrivals are produced as a result of phase conversion of P to S at the base of sediments. To understand whether all or only part of the delay time is caused by a sediment layer, the near range data (e.g. Fig. 3) was used to extract a near surface delay. Once the near surface delays were removed from the delay

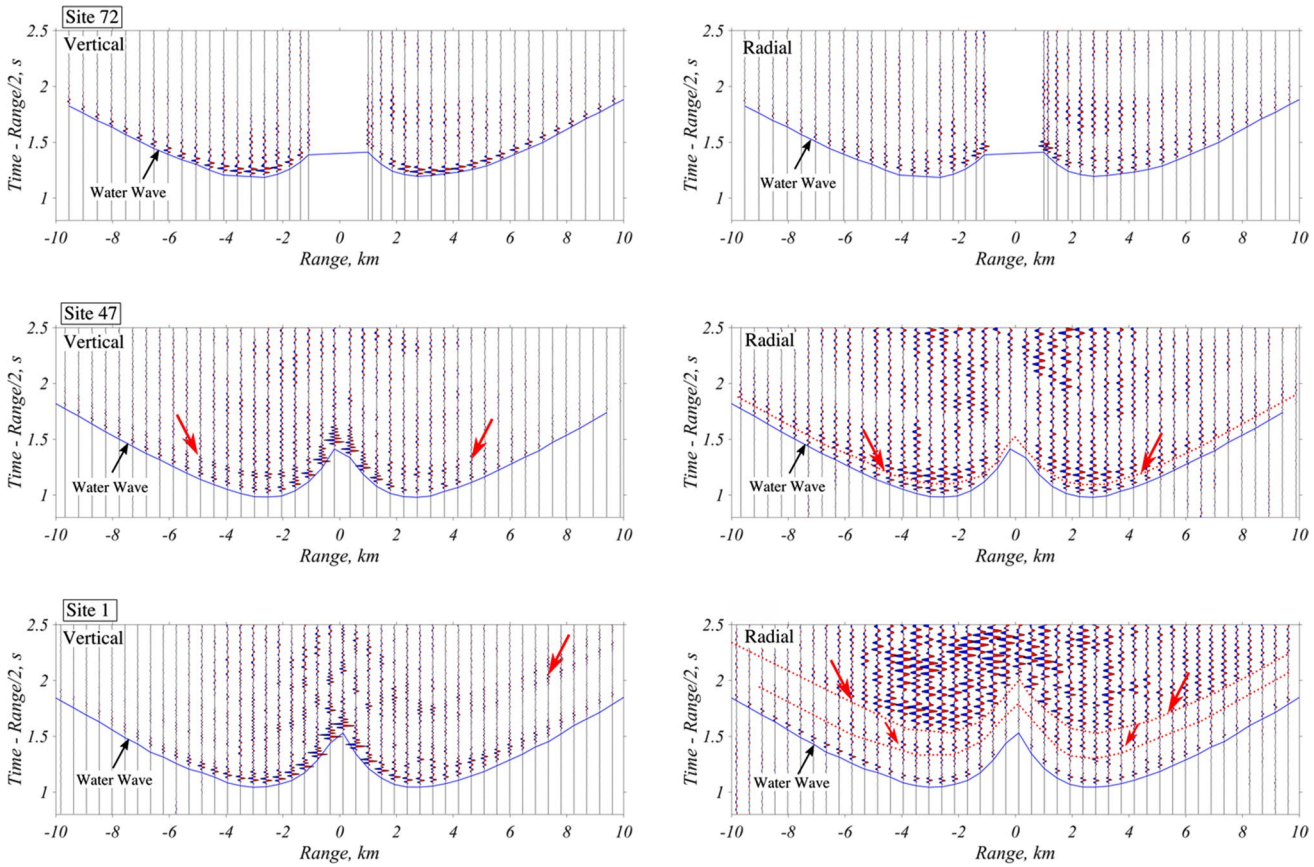

Fig. 3 Common receiver gathers, out to 10 km range, of the vertical (Z) and radial (R) components for three receivers. The corresponding source lines and receiver locations are given in Fig. 1b. (Top row) A station located 2 km from the axis of the spreading center and within Domain III. (Middle Row) A station located 11 km from the axis of the spreading center and within the transition zone. (Bottom Row) A station located 20 km from the axis of the spreading center and within Domain II. The water wave arrivals (blue line) and shear waves (red dotted lines and arrows) are marked in each plot. The data were band-pass filtered 15–35 Hz (Butterworth filter with 24 dB/octave attenuation roll off) and are amplitude adjusted by a factor of $(1+r)^{1.2}$ where r is the source-to-receiver range

times at longer ranges, the corrected delay times were used to estimate the interface depth of the phase conversion.

Methods and preliminary results

In the following two sections, P and S wave arrivals are examined at near "Near-range data" sect. and far "Far-range data" sect. ranges. To identify the seismic arrivals, we examined wave amplitudes and polarizations as a function of range using comparison with synthetic results. The near range data provides information on the shallow-most seismic structure, which is then used to correct the far-range data and determine deeper structure.

Near-range data

Preliminary traveltime modelling of the shear waves in the near range data (red arrows in Fig. 3) indicated that these high-amplitude arrivals, with traveltimes closely following the water wave at ranges up to 10 km, are of either PS or SS type (Fig. 2a). Here we show two possibilities. The first model mimics a low-velocity sedimented seafloor with a 40 m thick low-velocity layer ($Vp = 1.58$ km/s, $Vs = 0.3$ km/s) overlying a higher-velocity crustal layer. The second model mimics an un-sedimented seafloor with a shallow 110 m thick low-velocity crustal layer ($Vp = 2.2$ km/s, $Vs = 0.7$ km/s). In the first model, traveltimes of SS and PS phases match observed traveltimes of 'water-wave-parallel' arrivals, whereas in the second model travel times of SS phases match the observed traveltimes. In the simplest scenario, there are three unknowns, Vp, Vs, and layer thickness, requiring at least three pieces of information, such as the travel times of P–P, S–S, and P–S waves and their multiples. This requires careful phase identification using wave polarization information and amplitudes, and traveltime move-out in order to model the seismic structure around each station.

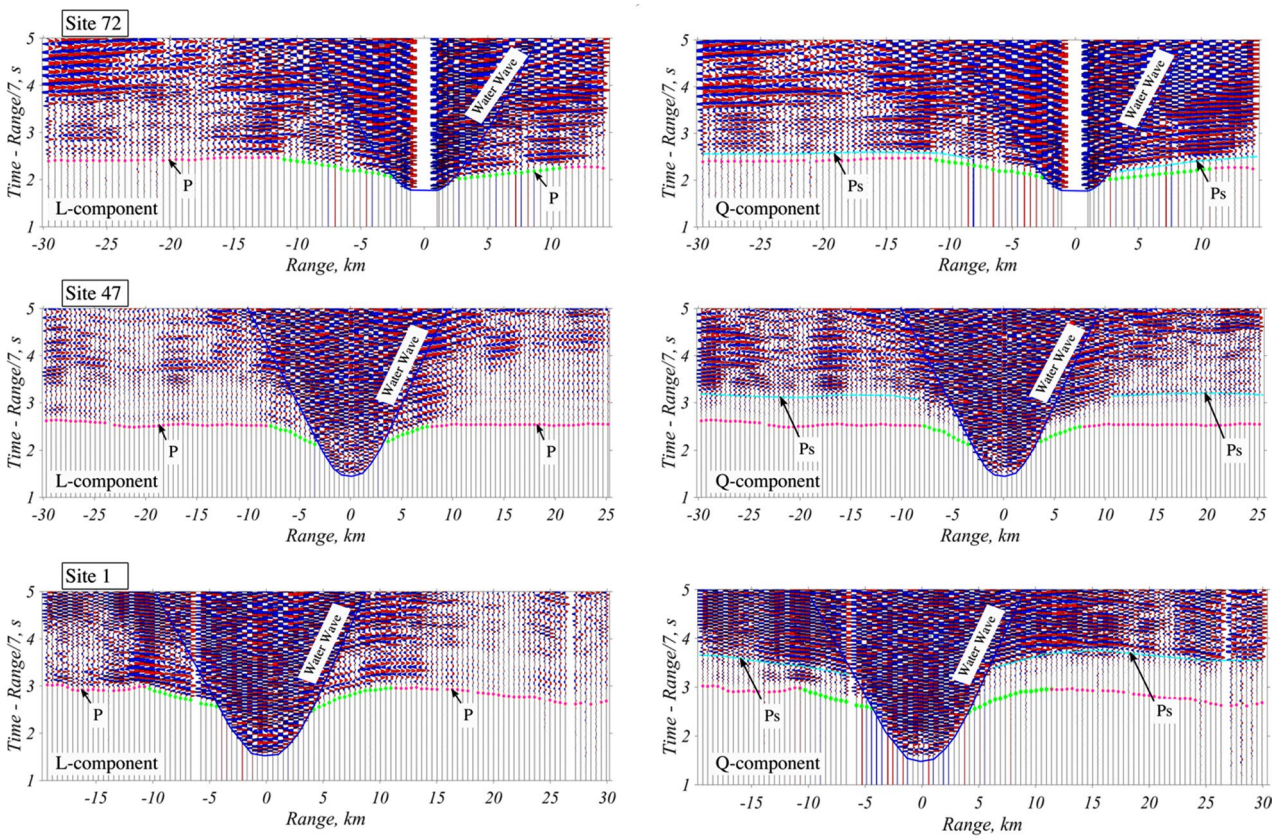

Fig. 4 Common receiver gathers of L and Q component traces to 30 km range. From top to bottom, these are the same receivers shown in Fig. 3. Upper crustal (green dots) and lower crustal (pink dots) P-wave refractions are strongly observed on the L component. For reference, these arrivals are also indicated on the Q-component records. The water wave arrivals are indicated by a blue line. The records are displayed with a reduction speed of 7 km/s, so that lower crustal refractions and their multiples appear approximately horizontal. The data were bandpass filtered 2—15 Hz (Butterworth filter with 24 dB/octave attenuation roll off) and are amplitude-adjusted by a factor of $(1+r)^{1.2}$ where r is the source-to-receiver range

We used solutions (Fig. 5) to the Zoeppritz equations (Zoeppritz 1919) to estimate variations in amplitude of P and SV phases with source-receiver range (and ray parameter) for an incident water wave at the seafloor. The same models were compared as before ($Vp = 1.58$ km/s, $Vs = 0.3$ km/s, $\rho = 2100$ kg/m^3 vs. $Vp = 2.2$ km/s, $Vs = 0.7$ km/s,

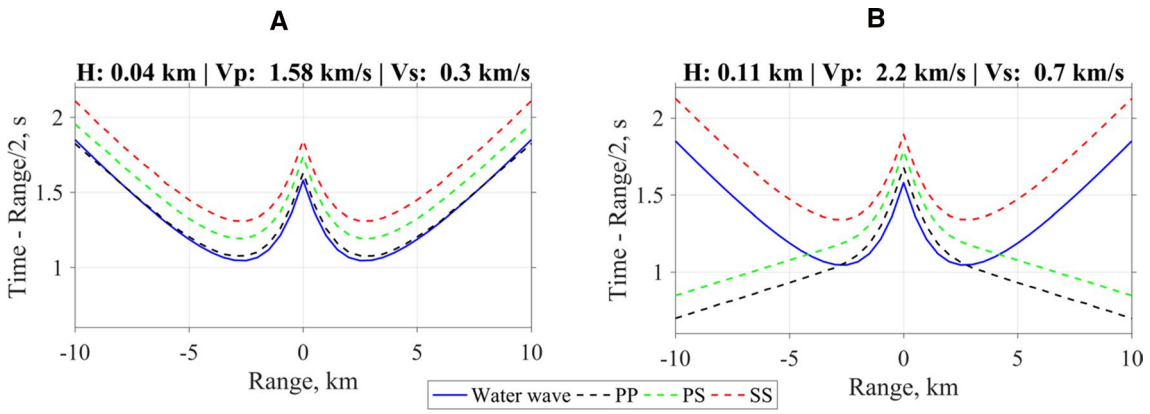

Fig. 5 Synthetic travel times versus range for the same source-receiver geometry in Fig. 3. (**a**) For a low-velocity seafloor and (**b**) for a high-velocity seafloor. Medium properties are shown on each plot. The phases PP, PS and SS are defined in Fig. 2

$\rho = 2300$ kg/m^3). Density was determined from the relation $\rho = 1.85 + 0.165Vp$ (Christensen and Shaw, 1970). For a downgoing water wave, Fig. 6 shows the efficiency of P-to-S conversions for the two seafloor types. Figure 6a shows the corresponding ray diagram and standard nomenclature. For a low-velocity seafloor (Fig. 6b), the transmitted P wave (dashed blue line) has an amplitude that is ~ 60% of the incident wave within the critical ray parameter, as opposed to ~ 45% for a high-velocity seafloor (solid blue line). Critical incidence, defined by a 90º refraction angle ($= \sin^{-1}(Vp_w/Vp_1)$), is marked by a local drop in S amplitude and a jump in P wave amplitude. Due to the inverse relation of critical angle with seafloor velocity, the critical incidence is reached at a smaller angle (smaller ray parameter) and hence at a shorter range for a high-velocity seafloor as compared to a low-velocity seafloor. Conversion from P-wave phase to S-wave phase is greatest post critical incidence of the water wave (red lines). The amplitude of the P-to-S conversion is observed to increase with the angle of incidence of water waves in both cases. At post critical incidence, the low velocity seafloor produces a ~ 50% lower amplitude coefficient for the converted wave, as compared to the high-velocity seafloor case. In addition, the amplitude of converted waves increases post critical incidence, with stronger conversion for high-velocity seafloor. In summary, a high-velocity seafloor produces a relatively strong downgoing P-to-S conversion for post-critical incidence (roughly 2.7 km range in 3 km of water), while a low velocity seafloor produces a weak conversion at all ranges. Considering that the water–sediment interface may have even more gradual increase in properties than modelled here, it is likely that a sedimented seafloor does not produce a strong P-to-S conversion of the downgoing water wave.

P-to-S conversions could also occur at the base of a sediment layer or at deeper layer interface. To further understand converted waves and their amplitude variation with range as a function of seafloor type, we numerically modelled waves from a point source travelling into a layered velocity model. A finite difference numerical solution to the stress-velocity coupled wave equation (Levander 1988) was used to model phase converted reflections from an interface below the seafloor. The 1-D model (Fig. 7h, i) consisted of a 2400 m thick water layer, a 1-km-thick upper crustal layer, and a lower halfspace. The time and space steps were set to 0.001 s and 0.03 km respectively. In the first case, the velocities and density of the layer are ($Vp_1 = 1.58$ km/s, $Vs_1 = 0.3$ km/s, $\rho_1 = 2100$ kg/m^3) and the lower halfspace is set to ($Vp_2 = 3$ km/s, $Vs_2 = 1$ km/s, $\rho_2 = 2400$ kg/m^3) (Fig. 7h) to mimic a sediment to layer 2A transition. In the second case, the velocities and density of the layer are ($Vp_1 = 2.6$ km/s, $Vs_1 = 1$ km/s, $\rho_1 = 2300$ kg/m^3) and the lower halfspace is set to ($Vp_2 = 4$ km/s, $Vs_2 = 2$ km/s, $\rho_2 = 2500$ kg/m^3) (Fig. 7i) to mimic a layer 2A-2B transition. The point source is located at the sea surface and the receivers are located on the seafloor with 500 m interval spacing.

For the case of a low-velocity seafloor, the water wave conversion into the subsurface as an S-wave is minimal (as described previously using the Zoeppritz equations'

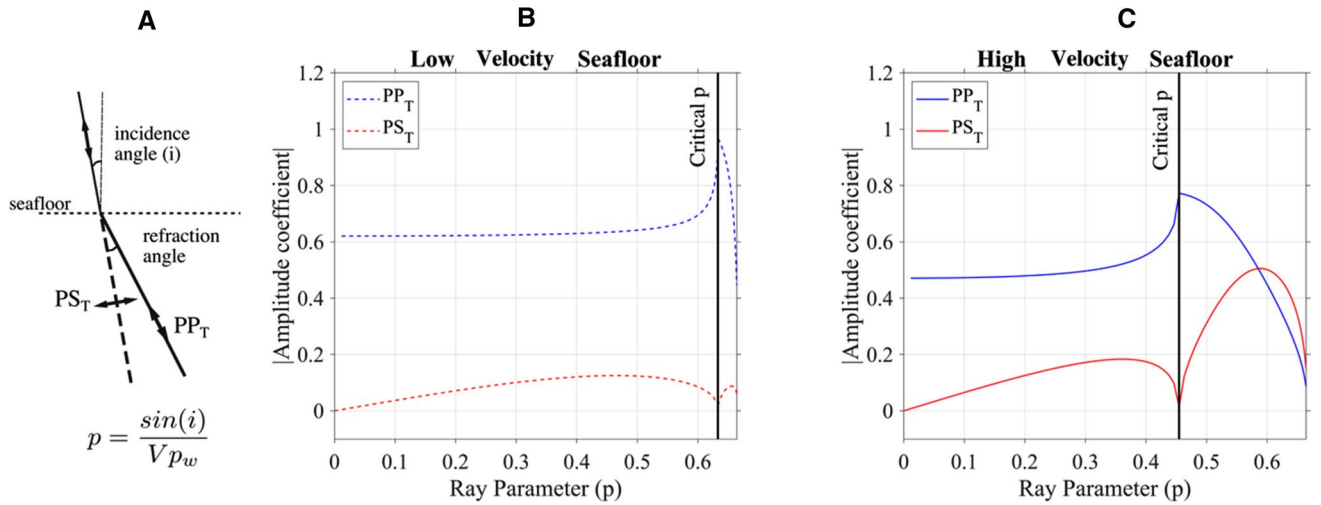

Fig. 6 Zoeppritz solutions for a downgoing wave. **a** Schematic ray diagram representing P-to-S conversion of a downgoing water wave at the seafloor for a specific ray parameter, p, related to incidence angle by the given equation. **b** Relative amplitude of PP_T (blue) and PS_T (red) with respect to the water wave, as a function of ray parameter, for the two cases discussed in the text. Both cases have a water layer ($Vp_w = 1.5$ km/s, $\rho_w = 1000$ kg/m^3), underlain by a halfspace (dashed lines on left corresponds to case with a low impedance contrast, $Vp_1 = 1.58$ km/s, $Vs_1 = 0.3$ km/s, $\rho_1 = 2100$ kg/m^3, and solid lines on the right correspond to a higher impedance contrast, $Vp_1 = 2.2$ km/s, $Vs_1 = 0.7$ km/s, $\rho_1 = 2300$ kg/m^3). In both the cases, the vertical lines (solid or dashed) represents the ray parameter at critical incidence

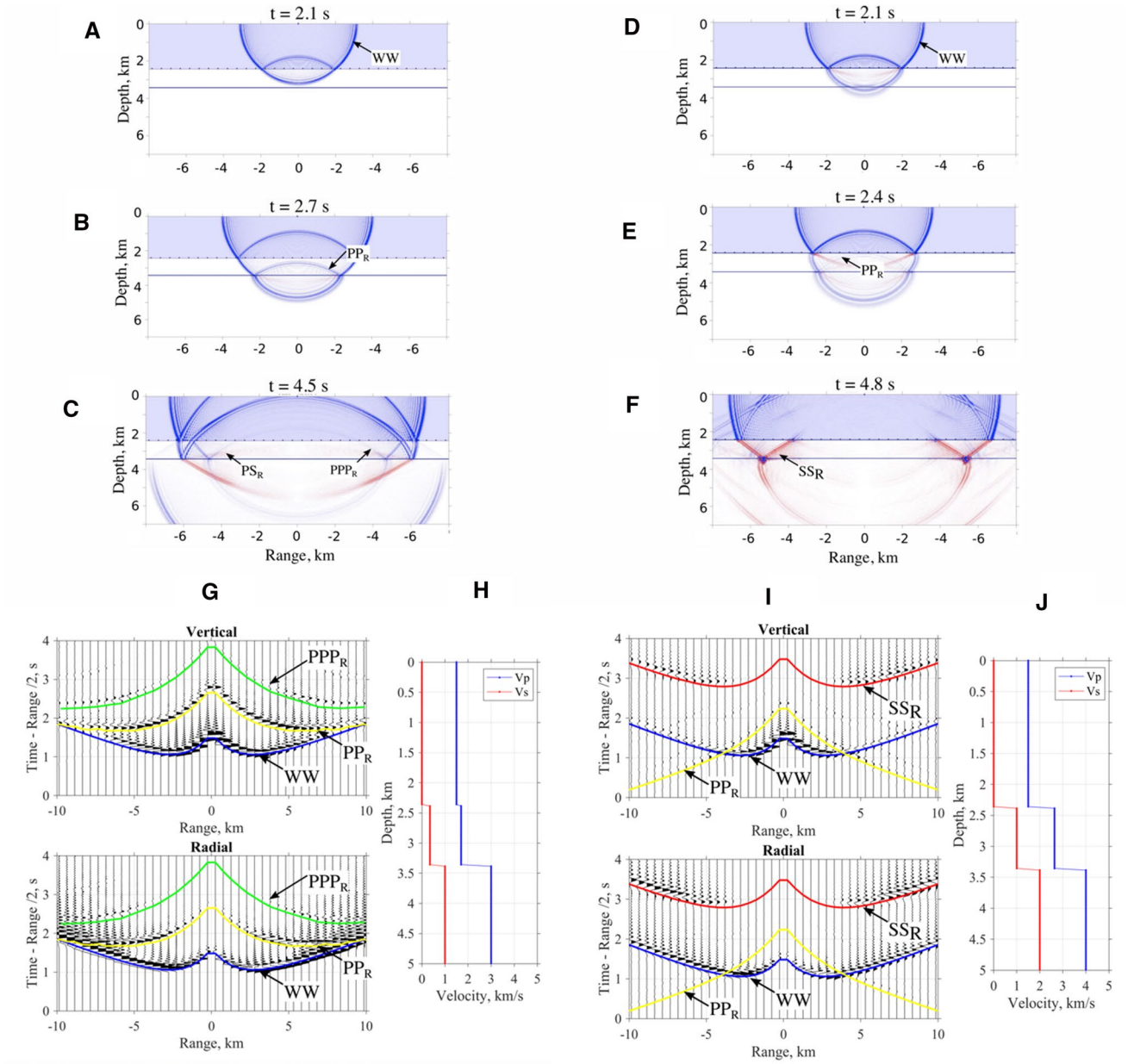

Fig. 7 Numerically simulated elastic wavefields and seismic source gathers for the two models shown in Fig. 6. A point source at (0,0) generates waves recorded by receivers located at the seafloor at 2.4 km depth with 500 m inter-spacing. Model properties are shown in (**h**) and (**j**) and the corresponding wavefields at different times are shown in (**a**–**c**) and (**d**–**f**) respectively. Labeled wavefields are direct water wave (WW), reflected P-wave (PPR), and reflected phase converted S-wave (PSR, SSR). (**g**) and (**i**) show common source gathers for the given source-receiver geometry in the top figures, for receivers up to 10 km range. Also overlying the gathers are traveltime curves of WW (blue), PPR (yellow), PPPR (green), and SSR (red) phases, obtained by ray tracing

solutions), and a stronger transmitted P-wave is observed (Fig. 7a, b). The transmitted P-wave is then reflected back more strongly from the subsurface interface as a P-wave (labelled PP_R), as compared to a reflected S-wave (labelled PS_R). Note that due to the difference in propagation direction, the PP_R phase is recorded with reversed polarisation with respect to the water wave on the vertical component (Fig. 7g). As the waves propagate, multiples of the P-wave within the sediment layer are observed (PPP_R) with little to no conversion from P to reflected S at the lower boundary. An important observation is a strong downgoing transmitted S-wave at the base of the sediment layer, which would be important to creating S–S reflections from deeper layers not included in this simulation.

In the second case, with a high-velocity seafloor layer, the water wave efficiently transmits into the subsurface as

a P wave, and as an S-wave at oblique incidence (Fig. 7d, e). This S-wave is reflected from the subsurface interface (SS_R) and is recorded on both vertical and radial components (being relatively stronger in the radial direction). The amplitude of SS_R is low to zero at ranges within critical values (< 2.5 km), and it increases at ranges > 2.5 km. The wave polarisation of SS_R is found to be the same as that of the water wave in the radial direction. The second prominent wave recorded by the receivers is the PP_R arrival, which is stronger on the vertical component and with reversed polarisation with respect to the water wave. The polarisation and amplitude variation with range of SS_R and PP_R phases were instrumental in identifying the arrivals in the real data. In all cases, ray tracing was able to predict the arrival times of each of the different observed phases, shown by the labelled lines in Fig. 7g, i.

While initial ray tracing indicated that the observed shear waves can be of PS_R kind, numerical modelling has shown that the PS_R wave has a very low amplitude as compared to an SS_R wave. Since high amplitude shear waves are observed consistently across the study area, examples of which are shown in Fig. 3, we interpret these waves as SS_R waves, where the P-to-S conversion is likely occurring at the seafloor in the absence of appreciable sediments. In the presence of appreciable sediments, the P-to-S conversion is most likely to occur along the downgoing ray path at the base of sediments (referred to as a pSS_R wave, where the path "p" is within the sediments), since a P-to-S conversion at the water–sediment interface is not likely to be efficient. Further traveltime modelling suggest that greater sediment thickness (> 50 m) will decrease the overall traveltime of the wave and not produce the observed 'water-wave parallel' arrivals. Hence we say that the sediment layer, within the bounds of our experiment, is generally thinner than 50 m, and the observed PP and SS phases are reflections from a sub-basement interface.

PP and SS traveltime picks were used in a grid search for the average S-wave velocity, Vs_1, and reflector depths, H_1, that minimized the misfit between observed and calculated traveltimes. Results of these calculations (discussed in "Results" sect.) provide a mean layer thickness of 70 m and a mean Vs of 570 m/s, across the study area. The listing for each station is given in Online Resource 3. The error in estimating Vs_1 and H_1 due to pick error is under 12% (50 ms pick uncertainty). The calculations employed an estimate of the P-wave velocity under each station, taken from Dunn et al. (2013). These are estimated to have 20% uncertainty, producing a 20% uncertainty in Vs_1 and H_1. Drawing from the rule of uncertainty in product and quotient of two variables, the overall uncertainty in Vs_1 and H_1 is 32% which will turn out to be acceptable for the observed values of Vs_1 and H_1.

Far-range data

We first considered whether the far-range upgoing Ps phase could have its conversion point at the shallow interface described in "Near-range data" sect. However, the traveltime delay caused by the near surface layer greatly underpredicts the traveltime delay observed between the P and Ps phases. Hence the conversion interface for the far range data must be deeper in all cases than the shallow interface, such as a layer 2A/2B transition. We performed a preliminary analysis using the solutions to Zoeppritz equations on the relative amplitude of P-to-S converted wave at the base of a volcanic layer with respect to the upgoing P-wave (Fig. 8a). Assuming fixed Layer 2B properties ($Vp_3 = 4.5$ km/s, $Vs_3 = 2.5$ km/s, $\rho_3 = 2600$ kg/m^3), the upper crustal properties, Vp_2, Vs_2 and ρ_2, were varied (refer to caption of Fig. 8). Estimates of the incidence angle of crustal refractions at the station (from polarisation analysis) provides a rough estimate of the range of possible ray parameters for Ps phase conversion (Fig. 8b). Within this range of interest, the P-to-S conversion is more efficient as the ray parameter, or incidence angle, of the upgoing wave increases, and the converted wave's amplitude is greater for greater velocity contrasts between the lower and upper layers.

Since more information about the Ps phase and its multiples (Fig. 9a) is required to get a unique estimate of layer thickness (H_2) and Vp/Vs value in this layer, we again used solutions to Zoeppritz equations to identify the most strongly arriving waves. We modelled the amplitude ratios with respect to crustal (P-wave) refractions, as shown in Fig. 9b. The lower medium was simulated as seismic layer 2B ($Vp_3 = 4$ km/s, $\rho_3 = 2600$ kg/m^3, $Vs_3 = 2.2$ km/s) while the upper medium was simulated as seismic layer 2A ($Vp_2 = 2.5$ km/s, $\rho_2 = 2200$ kg/m^3, $Vs_2 = 1.2$ km/s). As the ray parameter increases, the P-to-S conversion becomes more efficient, while P-reverberation (Pppp) amplitudes decrease. In terms of the traveltimes of these two phases, they interfere with each other when the Vp/Vs ratio is close to 3. They can be differentiated from each other based on their relative amplitudes on the vertical (or L) and radial (or Q) components. Amongst the shear wave multiples shown in Fig. 9a, the Ppps phase is fastest to arrive, high in amplitude, and inverted in polarity. These observations helped identify Ps and Ppps phases in the radial component of the data.

Using the simple traveltime formulas given by Eqs. 1–2, we inverted for the layer thickness (H_2) and interval velocity (Vs_2) in the upper layer, which produced the phases Ps and Ppps.

$$\Delta t_{Ps} = H_1\left(\frac{1}{Vs_1} - \frac{1}{Vp_1}\right) + H_2\left(\frac{1}{Vs_2} - \frac{1}{Vp_2}\right) \quad (1)$$

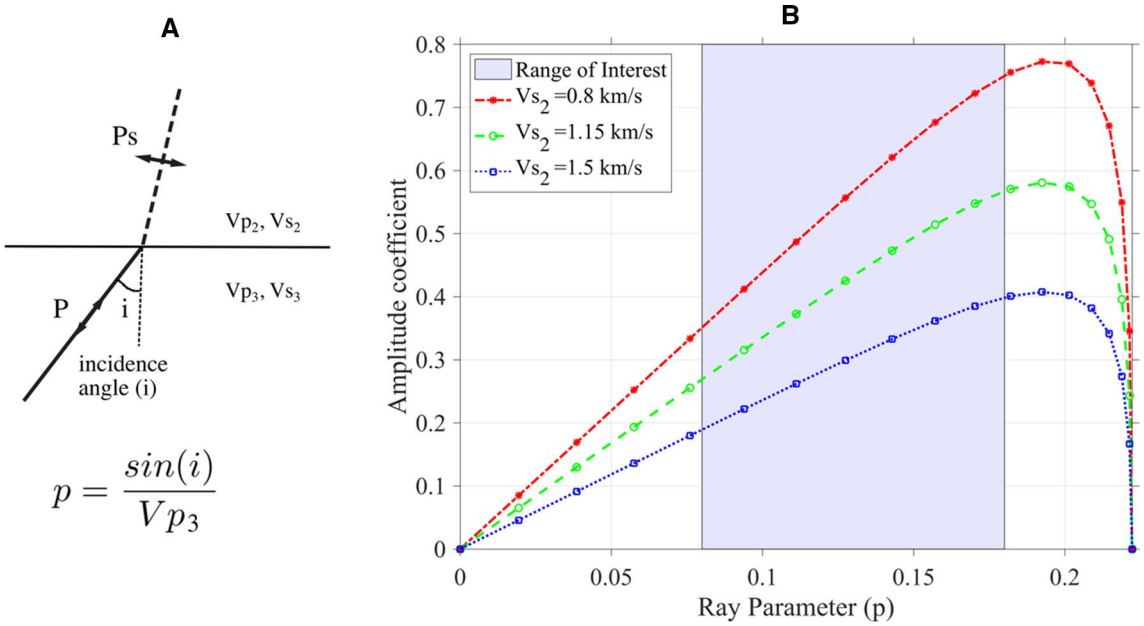

Fig. 8 Zoeppritz solutions for an upgoing wave. **a** Schematic ray diagram representing P-to-S conversion of an upgoing crustal refraction at the base of layer 2A. **b** Relative amplitude of Ps with respect to the P phase at different ray parameters (related to incidence angle by the equation in **a**). Properties in the lower halfspace are fixed to $Vp_3 = 4.5$ km/s, $Vs_3 = 2.5$ km/s, $\rho_3 = 2600$ kg/m^3. Transmission into the upper halfspace with increasing medium impedance properties is shown: red ($Vp_2 = 2.6$ km/s, $Vs_2 = 0.8$ km/s, $\rho_2 = 2230$ kg/m^3), green ($Vp_2 = 2.9$ km/s, $Vs_2 = 1.15$ km/s, $\rho_2 = 2330$ kg/m^3) and blue ($Vp_2 = 3.3$ km/s, $Vs_2 = 1.5$ km/s, $\rho_2 = 2400$ kg/m^3). The range of ray parameters shown by the blue shaded region correspond to observed ray parameters of the incident P-wave at the receiver

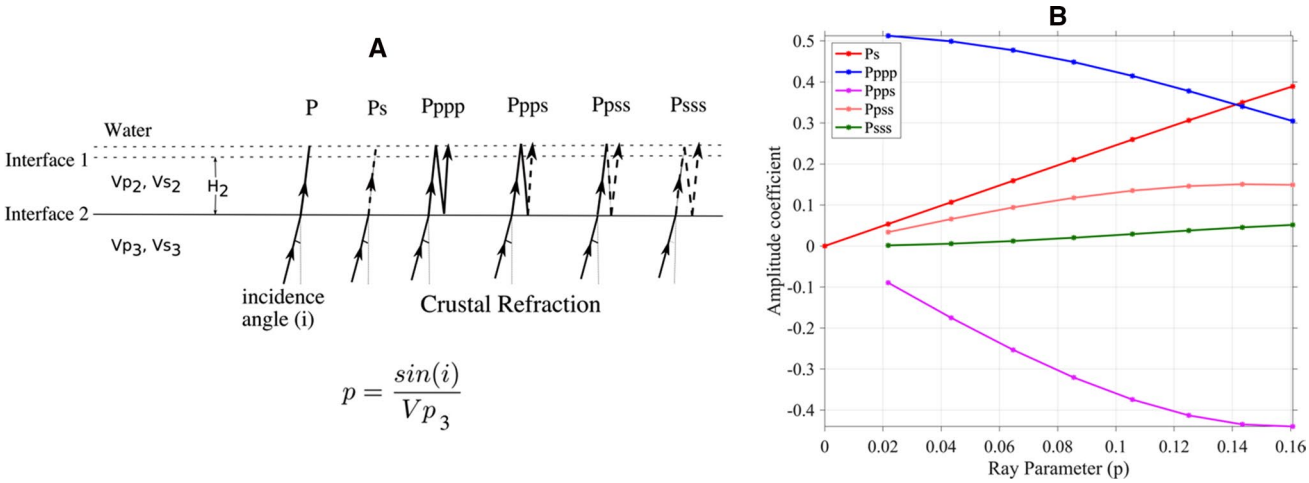

Fig. 9 Zoeppritz solutions for an upgoing wave and its multiples. **a** Schematic ray diagram representing P-to-S conversions of an upgoing crustal refraction and its multiples. Solid lines represent P-waves and dashed lines represent S-waves. **b** Relative amplitudes (as compared to the incident P wave) of converted wave primaries and multiples defined in **a** as a function of ray parameter. Properties in the lower layer and upper layer are fixed at $Vp_3 = 4$ km/s, $Vs_3 = 2.2$ km/s, $\rho_3 = 2600$ kg/m^3 and $Vp_2 = 2.5$ km/s, $Vs_2 = 1.2$ km/s, $\rho_2 = 2200$ kg/m^3 respectively

$$\Delta t_{Ppps} = H_1\left(\frac{1}{Vs_1} + \frac{1}{Vp_1}\right) + H_2\left(\frac{1}{Vs_2} + \frac{1}{Vp_2}\right) \quad (2)$$

Δt_{Ps} and Δt_{Ppps} are defined as the delay time with respect to crustal refracted P-wave in observed data. The near surface properties (H_1, Vp_1, Vs_1) were calculated as described in "Near-range data" sect. The P-wave velocity in the lower layer (Vp_2) was approximated from prior tomography results (Dunn et al. 2013). Due to the intermittent nature of Ps and Ppps phases, they were recorded with acceptable

signal-to-noise ratios at only 36 receivers spread across the study area.

Uncertainty in the estimates of *Vp*/*Vs* value and layer thickness (*H*) using the method described above is found to be modestly dependent on *Vp* uncertainty. For example, using a *Vp* of 3 km/s and a *Vp*/*Vs* ratio of 2 for a 800 m layer, the uncertainty in H_2 is given by

$$\Delta H_2 = \left(\frac{\partial H}{\partial Vp_2}\right)\Delta Vp_2 = 0.27\Delta Vp_2 \tag{3}$$

which means the uncertainty in H_2 is less than ~ 50 m for a 0.2 km/s uncertainty in Vp_2. The error contribution from a picking error of 0.05 s was found to be within 15% for H_2 and less than 10% for *Vp*/*Vs* values. Equations (1) and (2) assume vertical ray paths. Inserting appropriate values into the following equation (Zhu and Kanamori, 2000):

$$H = \frac{t_{Ps}}{\sqrt{\frac{1}{v_s^2} - p^2} - \sqrt{\frac{1}{v_p^2} - p^2}} \tag{4}$$

and using a ray parameter range of 0.05 to 0.2, we find that ray bending has negligible effect (< 1 m).

Results

SS travel times from near offset data, which indicate variations in uppermost crustal and/or sediment layer properties (H_1, Vp_1, Vs_1), were compiled for all available stations and are shown in Fig. 10. Theoretically, SS-waves are not generated at zero range, hence for this figure the traveltimes along a hypothetical vertical ray path were computed from the layer thickness and velocity estimated from the wide-angle (2–10 km range) data for each station. The traveltime magnitude represents the combined effect of near surface S-wave velocities and the depth of the reflector, with larger SS times (larger circles in Fig. 10) corresponding with either lower Vs_1 values and/or a greater values of H_1. In general, smaller times are observed near the ridge, and larger times are observed away from the ridge, with some particularly large values for stations located on the east side (arc side) of the ridge axis. Also shown in Fig. 10 is a sonar image of the seafloor for the study area (Dunn, 2015). Smaller SS times are observed in regions with higher sonar backscatter (usually younger, un-sedimented seafloor), and larger SS times are observed in areas of very low backscatter (e.g. heavily sedimented seafloor). There is a greater range of both SS times and backscatter values on the east side, where backscatter and seafloor morphology indicate larger variations in sediment cover due to sediment ponds, topographic effects, and late stage volcanism. The largest travel times correlate with basins that appear to be filled with sediments.

Figure 11 shows a plot of estimated values of H_1 as function of distance to the ridge axis; the markers are differentiated based on the respective station's location within the crustal domains. In general, larger H_1 values are found farther from the ridge, with a greater range of values on the east side. Furthermore, the average value of H_1 is greater on the eastern side of the ridge axis (~ 100 m) as compared to the west (~ 60 m). The smallest non-zero values of H_1, ~ 50 m, are found within 4 km of the ridge axis. Some stations do not have an estimated H_1 value due to no discernible PP wave and do not appear in Fig. 11. The average S-wave velocity is relatively lower on the east side (~ 500 m/s) than the west side (~ 570 m/s); both being higher than values observed in pelagic and hemipelagic marine sediments (200–300 m/s; Hamilton 1979), and lower than values observed in consolidated volcaniclastic sediment (0.8–1 km/s; Kenter and Ivanov 1995) or layer 2A (1.5–2 km/s; Spudich & Orcutt 1980).

Few independent estimates of sediment thickness in the region are available. ROV images detect little to no sediment near the ridge axis (Ferrini et al. 2008). Backscatter images also indicate a sediment-free spreading center, with increasing sediment coverage at greater crustal ages and greater coverage on the arc-side of the ridge (Martinez et al. 2006). In the off axis regions, sub-bottom profile data from recent cruises to the area do not penetrate to basement in sedimented regions and thus can only provide crude estimates of minimum sediment thickness. Log data from a station located 50 km west of the ridge axis, in Domain III, found a ~ 20 m sequence of clayey nannofossil oozes with interbedded turbiditic volcanic sands and silts, pyroclastic ashes, and thick-bedded mafic hyaloclastites overlying a MORB-like igneous basement (Hawkins 1994), suggesting sedimentation on the western side of the ridge is not heavily influenced by arc volcanic debris. Examining the backscatter and topography together, and estimating the degree of sedimentation from the degree of in-filling of local topography, suggests that the western side of the ridge within the seismic array is only lightly draped by sediment with increasing age, whereas the eastern side is more heavily draped with some broad valleys with significant accumulation. Based on our seismic observations and drawing inferences from all available information, we conclude that the sediment cover on the western side of ridge axis is generally less than 20 m thick, and gradually reduces to zero towards the ridge axis as the seafloor becomes younger. On the eastern side of ridge axis, sediment cover is variable, ranging between 0 and 50 m, with the exception of some deeper sediment ponds, where it could be substantially thicker.

While the travel times of waves are influenced by the sediment thickness, it is clear that the S–S reflection depth is not the base of a sediment layer, since it occurs even where little to no sedimentation is found. This near surface layer (of

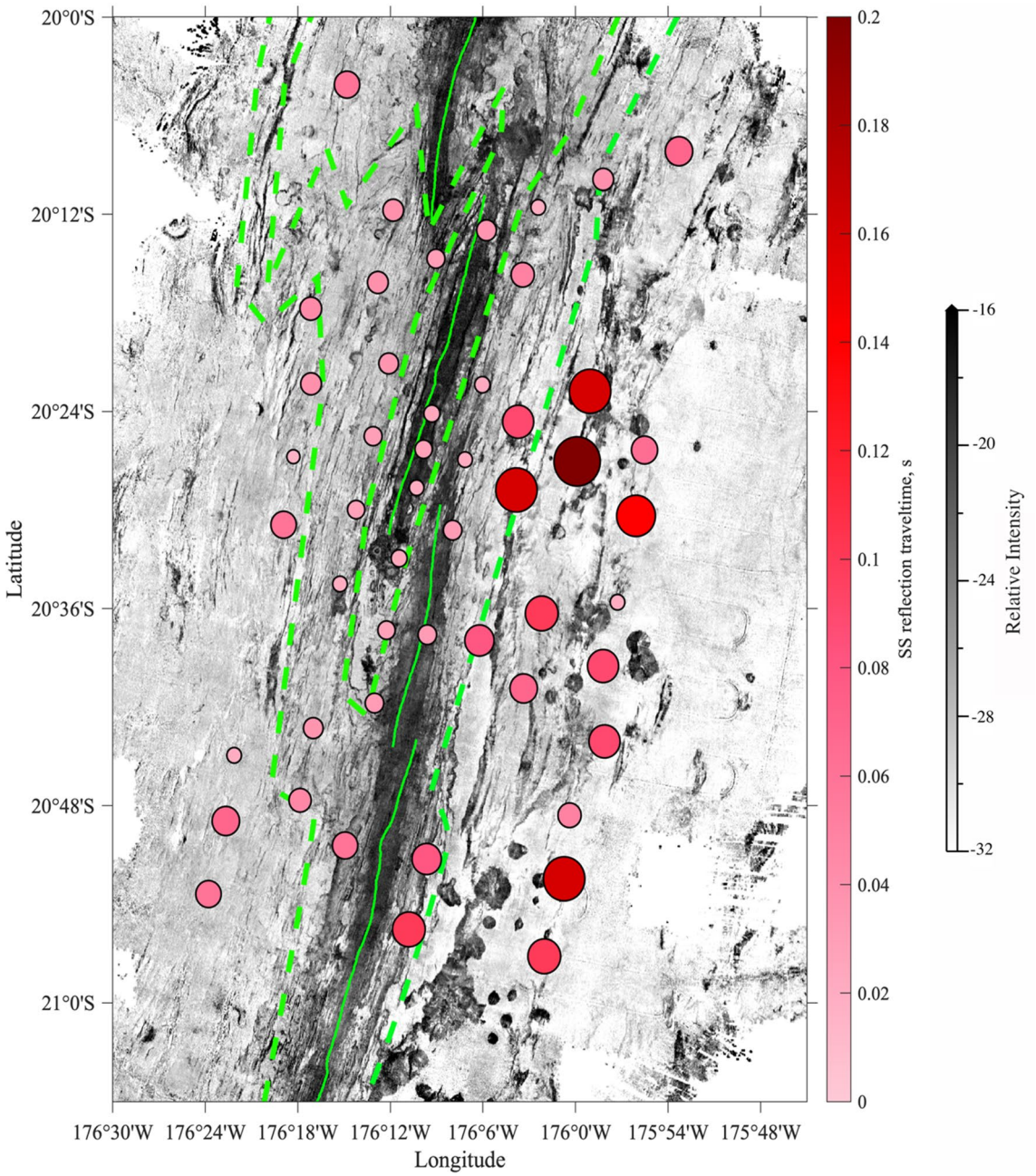

Fig. 10 Sonar image of the study area and observed SS traveltimes for each station. The size of each circle is proportional to the estimated vertical, two-way-traveltime for the layer thickness and velocity estimated from the near-range (2–10 km) data. The axis of the spreading center is shown by a solid green line, and the different crustal domains are separated by dashed green lines. In the sonar image (from Dunn, 2015), darker colors indicate higher sonar return (e.g. young un-sedimented seafloor) and lighter colors indicate lower sonar return (e.g. heavily sedimented seafloor)

thickness H_1) is a low-velocity surface layer within the igneous crustal layer 2A. Away from the ridge axis, in the presence of sediments, the reflections probably still occur at the base of an igneous layer, since the values are consistent with near-axis values plus an additional effect due to sediment. In any case, the base of this layer is too shallow to be consistent with a layer 2A/2B boundary (Jacobs et al. 2007). Note that P-waves reflecting from the base of such a thin layer would arrive within < 50 ms of the seafloor reflection in multi-channel seismic data, making the reflector difficult to observe in reflection images. S waves, on the other hand, arrive ~ 200 ms behind the water wave, providing enough phase separation for these reflected arrivals to be obvious in most cases. At 20 Hz, S waves also have much smaller wavelengths (~ 20 m) than

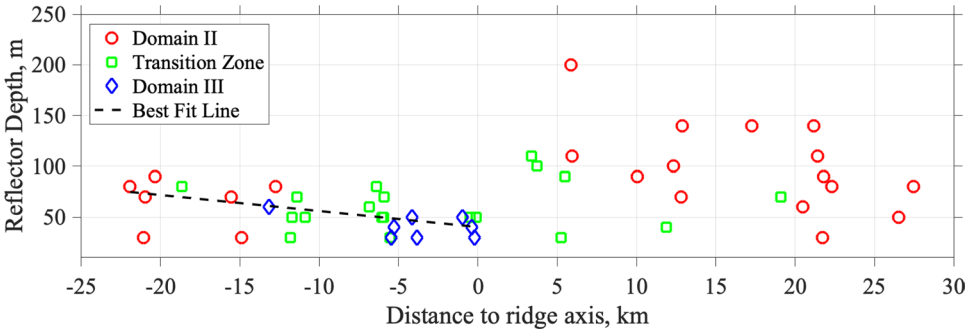

Fig. 11 Reflector depths (in m) beneath a station versus a station's distance to the ridge axis for the different crustal domains: Domain II (red), Transition Zone (green) and Domain III (blue). Also shown is the best fit line, made using a robust regression fitting method (Holland and Welsch 1977), through the data on the western side of the ridge axis

corresponding P waves (~100 m), enhancing their ability to be reflected from the bottom of a thin (<50 m) surface layer rather than pass across it.

When interpreting the far-range crustal refracted and converted arrivals (Fig. 4), the traveltime delays between P and Ps phases were 0.13–0.58 s greater than delays calculated from the near-surface layer properties (H_1, Vs_1, Vp_1). Therefore, P-to-S conversion depths of the Ps arrivals must be deeper than H_1. Using the method described in "Far-range data" sect., we found that Ps and Ppps arrivals were explained by a conversion (Ps) and subsequent multiple generation (Ppps) at depths (H_2) consistent with a layer 2A to 2B transition. Estimated depths for the 2A/2B transition (~500–700 m) are consistent with those determined by Jacobs et al. (2007), where available (primarily along the ridge axis).

Figure 12a shows estimated layer 2A thickness values overlain on a map view tomographic slice of upper crustal P-wave velocities (Dunn et al. 2013). In general, layer 2A is observed to be thicker in regions of low P-wave velocities and thinner in regions of higher P-wave velocities, roughly corresponding to the crustal domain designations. Figure 12b shows estimated *Vp*/*Vs* values in layer 2A overlain on a map view tomographic slice of upper crustal P-wave velocities. *Vp*/*Vs* values greater than 2.6 (red colors) are observed to spatially correlate with regions of low P-wave velocities. *Vp*/*Vs* values less than 2.6 (blue colors) are observed to spatially correlate with regions of high P-wave velocity. The correlation between layer 2A thicknesses, *Vp*/*Vs* values, and crustal domains is further demonstrated in Fig. 13, where thinner layers (~500 m, on average) with lower *Vp*/*Vs* (~2.3, on average) are found in Domain III and thicker layer values (~650 m, on average) and higher *Vp*/*Vs* (~3.0, on average) are found in Domain II. A list of estimated *H* and *Vs* values for each station is given in Online Resource 3.

Discussion

Near surface layer 2Aa

Across the seismic experiment, for areas either with or without appreciable sediment cover, our analysis points to the existence of a shallow low-velocity layer at the top of the crust. The low efficiency of P-to-S conversions at the top of sediment indicate a deeper source for the conversion point and an even deeper intra-crustal point for the observed S–S reflection. Therefore we suggest that the conversion point for P-to-S waves is at the top of the igneous crust, even in sedimented regions, and the S-to-S reflection horizon is within the igneous crust. The SS reflector is much shallower (~70 m on average) than estimated depths to the base of layer 2A (500–700 m; Jacobs et al. 2007). Arnulf et al. (2012), using a full waveform method for data collected along the Mid-Atlantic Ridge, also identified a thin (50–150 m thick) low-velocity crustal layer at the top of seismic layer 2A. They refer to this layer as seismic layer 2Aa, the name we adopt here. This layer could represent a more porous extrusive lava layer on top of a less porous lava layer below, where the difference arises perhaps due to a compaction process. For example, thin cracks created by thermal stresses during lava cooling are easier to close with increasing pressure than more spherical void space (Wilkens et al. 1991), perhaps allowing for a rapid change in seismic properties with increasing confining pressure at shallow depths, followed by a more gradual change at greater depth.

Layer 2A

The thickness of layer 2A is often considered to be a proxy for the thickness of the volcanic, extrusive layer of lavas at

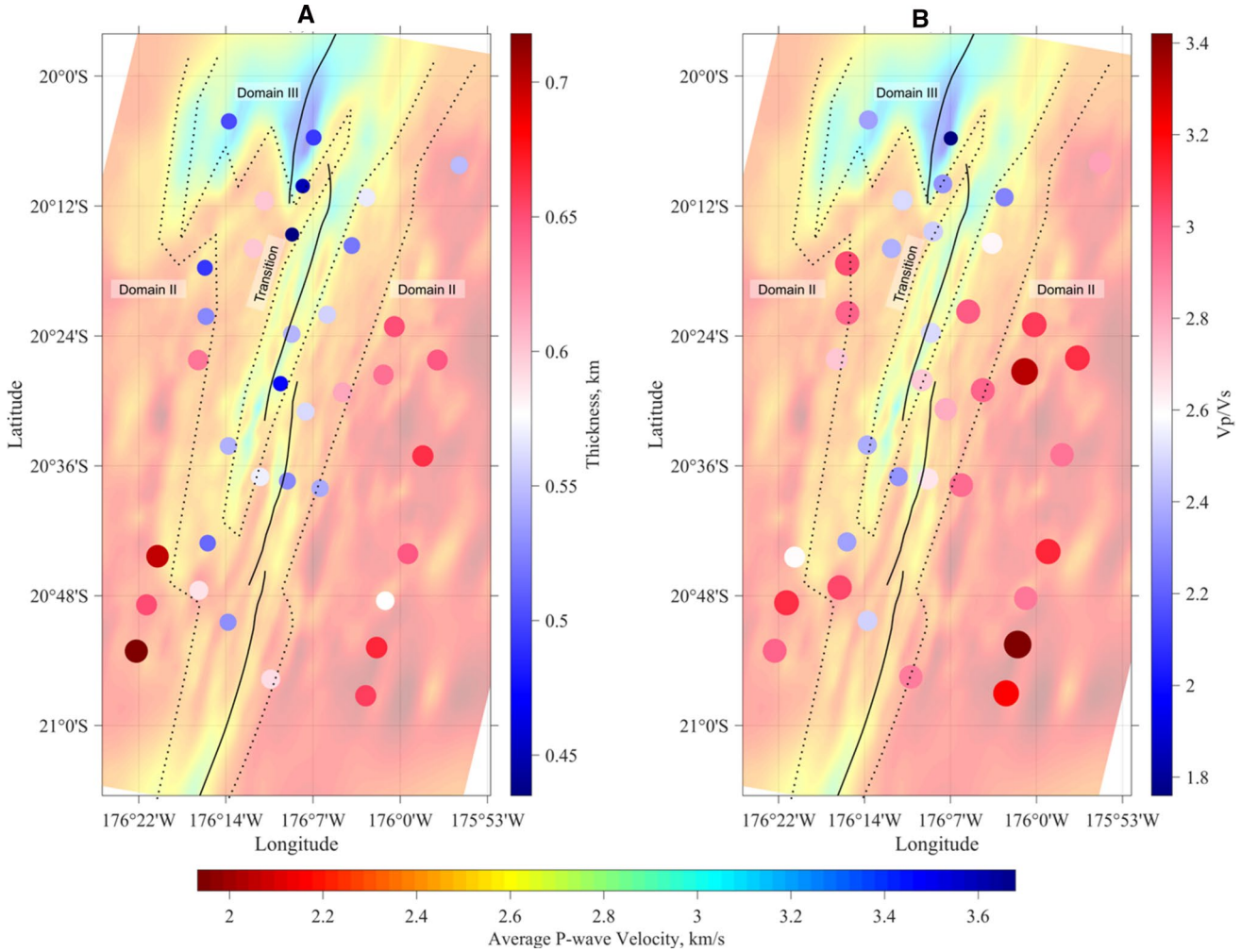

Fig. 12 Layer 2A estimated thicknesses **a** and *Vp*/*Vs* values **b** overlain on a map-view tomographic image of upper crustal P-wave velocities (from Dunn et al. 2013). The location of each circle corresponds to the location of the receiver. In the tomographic image, velocity values are averaged in the depth range of 250 m to 500 m of crust. The axis of the spreading center is shown by the thin black line. Only the values for 35 stations with recorded good signal-to-noise ratios for Ps and Ppps phases are shown

the top of the oceanic crust. In Domain II, where the crust is generally thicker (~ 8–9.5 km), layer 2A is also thicker (~ 650 m average), whereas the thinner crust in Domain III (~ 5.5–6 km) is capped by a thinner layer 2A (~ 500 m average). While it appears that a higher melt supply leads to a thicker volcanic layer in this area, the increase in layer 2A thickness with crustal thickness is not proportional, and the factors influencing the ratio of extrusive crustal growth to intrusive crustal growth are not clear. The rate of melt supply to the spreading center, the thermal structure of the crust, the eruptibility (e.g. density and viscosity) of the magma, and the depth to the crustal magma chamber may influence the volcanic layer thickness.

Estimated S-wave velocities correlate with the crustal domains. In Domain II, average *Vs* values are relatively low (~ 0.9 km/s), while estimates of *Vp*/*Vs* values (~ 3.0) and Poisson's ratio (υ) (~ 0.44) are relatively high. Conversely, in Domain III average *Vs* values are higher (~ 1.2 km/s), and estimates of *Vp*/*Vs* values (~ 2.3) and Poisson's ratio (~ 0.38) are lower. Poisson's ratio (υ) and *Vp*/*Vs* ratios are often used as an indicator of lithology (e.g. Christensen 1996; Collier and Singh 1998; Kim et al., 2018). Seismic velocities in layer 2A are thought to be largely controlled by porosity and the shapes of the voids and cracks (Shearer, 1988), with lower velocities in more porous rocks. Although a direct relationship of rock porosity with Poisson's ratio is non-unique, comparisons from different settings can help us understand their relative influence. For example, a seismic study by Collier and Singh (1998) on the ridge axis of East Pacific Rise found average Poisson's ratios of 0.34 in layer 2A. While this value is closer to our estimates for Domain III, Poisson's ratios in Domain II are much higher. A possible cause for the anomalously high Poisson's ratio in Domain II is thus higher porosity (e.g. Peacock et al., 2011),

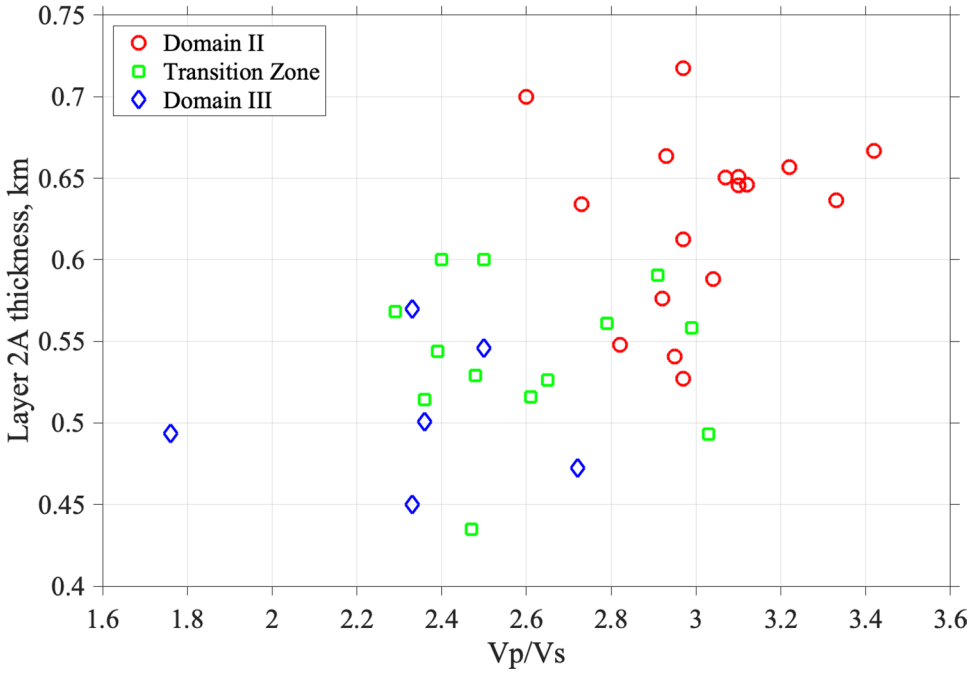

Fig. 13 Scatter plot of layer 2A thickness (in km) versus *Vp/Vs* across the study area, highlighting differences between the crustal domains

which is corroborated by the more vesicular nature of lava samples dredged from Domain II crust (Pearce et al., 1994).

In addition, the observed variations may also be controlled by major element composition. Jacobs et al. (2007) estimated that approximately half of the observed decrease in P-wave velocity in layer 2B (0.6 km/s), along the ridge axis could be attributed to compositional variations, while attributing the other half to a change in intrinsic porosity. Major element compositions for lavas sampled along the ridge axis change from basaltic to basaltic-andesite as the distance to the arc decreases. Our *Vp/Vs* values change approximately with this trend, although most of the major element trend along the ridge axis extends beyond the study area. However, our maps of *Vp/Vs* show significant major element chemistry changes extending into the off-axis areas. Domain II may have a basaltic-andesite cap of lavas as compared to basaltic lavas in Domain III. Whether due mostly to porosity changes or to porosity and major element changes is not clear in the absence of off-axis lava samples of crust formed at the spreading center, nevertheless the patterns in the seismic (and other geophysical data) are clear and suggest significantly different crustal formation processes in the near arc regions versus distal regions (Fig. 14).

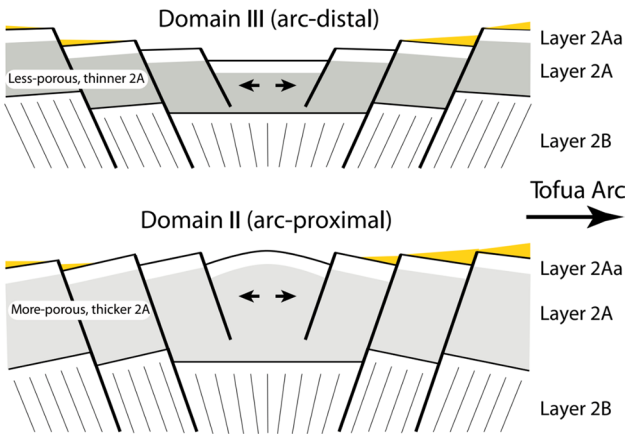

Fig. 14 Cartoon interpretation of upper crustal structure as a function crustal domain and arc proximity. A shallow seismic layer, 2Aa, is present across the study area and variably covered by thin sediments, which increase in thickness with lithospheric age and arc proximity. Layer 2Aa may represent a highly cracked surficial layer of the crust. For crust produced when the ridge axis was closer to the active arc (Domain II), a thicker and more porous lava layer (seismic layer2A) with a relatively more felsic composition is present. Away from the arc (Domain III), the crust is capped by a thinner and less porous lava layer with a basaltic composition

Subduction influence on upper crustal structure

In a mid-oceanic ridge system, decompression melting is the main source of magma production, wherein convection driven mantle material experience a decrease in pressure which leads to partial melting. Hence seafloor spreading rate, a primary factor driving convection, plays an important role in magma production and crustal formation. On the other hand, in a back arc setting, slab-derived volatiles (mainly water) reduce mantle melting temperature leading to enhanced melt production. Along the ELSC, the added effect of hydrous flux melting may produce up to ~ 30% more crust (Arai and Dunn 2014), and differences in magma supply and subsequent crustal structure are related to distance from the

arc volcanic front, rather than spreading rate (Martinez et al. 2006). Our estimates of layer 2A thickness and shear wave velocities in Domain II further strengthen this hypothesis. Since Domain II crust was formed when the ridge axis was closer to the volcanic arc, the volcanic layer shows a strong influence from slab-derived volatiles in the form of higher porosity (lower velocities and higher *Vp*/*Vs*). The presence of water during melting is expected to increase melt production (e.g. Davies and Bickle 1991; Stolper and Newman 1994). This is corroborated by the thicker volcanic layer in Domain II as compared to Domain III. In Domain III, faster velocities, lower *Vp*/*Vs*, and a thinner volcanic layer indicate a sharp decrease in the presence of slab derived volatiles. The interpretation is that the ridge has moved away from the influence of slab-derived volatiles when forming this type of crust.

Conclusions

In this study various P and S seismic phases, collected as part of the L-SCAN active-source seismic experiment, were used to investigate upper crustal structure across the Eastern Lau Spreading Center. The principle observations are:

(1) A shallow low-velocity layer of ~ 70 m thickness, on average, exists at the top of the igneous crust with *Vp*/*Vs* values in the interval of 2.7–5.8. This Layer 2Aa may be a highly-cracked and porous region of lavas on top of layer 2A and whose base is defined by a rapid change in elastic properties as thin, compliant cracks preferentially close under increasing lithostatic pressure.
(2) *Vp*/*Vs* in layer 2A is observed to be in the interval 1.7–3.4. In general, *Vp*/*Vs* is greater in Layer 2Aa than in Layer 2A across the study area.
(3) Seismic P and S waves and *Vp*/*Vs* vary across crust formed at the ELSC, forming a crustal-domain-specific pattern correlating with several previous geophysical and geological observations. Lower P and S velocities and higher *Vp*/*Vs* values (~ 2.8) exist in the upper oceanic crust in regions of crust that formed along the spreading center when it was located near the active Tofua arc. Higher P and S velocities, and lower *Vp*/*Vs* values (~ 2.6), exist in upper oceanic crust that formed relatively far from the active arc.
(4) The seismic observations indicate that a more porous and thicker volcanic layer of lava caps crust that formed when the spreading center was located near the active Tofua arc. Conversely, a thinner, less-porous layer of lava caps crust that formed further from the arc. In addition, the results are consistent with a change in silica-content of the lava layer with distance from the arc.

This study compliments previous studies of bathymetry, gravity, sonar backscatter, seismic structure and chemistry. The results show strong evidence for the influence of slab-derived water on crustal formation at the Eastern Lau Spreading Center when it is located closer to the arc, as compared to the waning influence on crust formed at locations away from the arc.

Acknowledgements This research was supported by a grant from the U.S. National Science Foundation (OCE16-34460). SOEST pub. no. 11107.

Authors contributions C. Lata performed the data analyses and wrote the manuscript, with guidance, input, and text editing by R. Dunn.

Funding National Science Foundation, Ocean Sciences Division.

Data availability The seismic data are available in the data repository at www.iris.edu.

Code availability FD code is available at www.mathworks.com.

Compliance with ethical standards

Conflicts of interest The authors declare that they have no conflict of interest.

References

Aki K, Richards PG (1980) Quantitative seismology. Freeman & Co, W. H

Anderson PN, Duennebier FK, Cessaro RK (1987) Ocean borehole horizontal seismic sensor orientation determined from explosive charges. J Geophys Res 92(B5):3573. https://doi.org/10.1029/JB092iB05p03573

Arai R, Dunn RA (2014) Seismological study of Lau back arc crust: mantle water, magmatic differentiation, and a compositionally zoned basin. Earth Planet Sci Lett 390(March):304–317. https://doi.org/10.1016/j.epsl.2014.01.014

Arnulf AF, Harding AJ, Singh SC, Kent GM, Crawford W (2012) Fine-scale velocity structure of upper oceanic crust from full waveform inversion of downward continued seismic reflection data at the lucky strike volcano, mid-atlantic ridge. Geophys Res Lett. https://doi.org/10.1029/2012GL051064

Austin, R.. 2012. "Early Seafloor Spreading and Variations in Crustal Accretion in the Lau Basin." MS Thesis, University of Hawaii. https://www.soest.hawaii.edu/GG/academics/theses/MS_2012_Austin.pdf.

Becker NC, Fryer P, Moore GF (2010) Malaguana-Gadao ridge: identification and implications of a magma chamber reflector in the southern mariana trough. Geochem Geophys Geosyst. https://doi.org/10.1029/2009GC002719

Bratt SR, Solomon SC (1984) Compressional and shear wave structure of the east pacific rise at 1120N constraints from three component

ocean bottom seismometer data. J Geophys Res. https://doi.org/10.1029/JB089iB07p06095
Christensen NI (1978) Ophiolites, seismic velocities and oceanic crustal structure. Tectonophysics 47(1–2):131–157. https://doi.org/10.1016/0040-1951(78)90155-5
Christensen NI (1996) Poisson's ratio and crustal seismology. J Geophysical Res Solid Earth 101(B2):3139–3156. https://doi.org/10.1029/95JB03446
Christeson GL, Kent GM, Purdy GM, Detrick RS (1996) Extrusive thickness variability at the east pacific rise, 9°–10°N: constraints from seismic techniques. J Geophysical Res Solid Earth 101(B2):2859–2873. https://doi.org/10.1029/95JB03212
Christeson GL, Purdy GM, Fryer GJ (1994) Seismic constraints on shallow crustal emplacement processes at the fast spreading east pacific rise. J Geophysical Res Solid Earth 99(B9):17957–17973. https://doi.org/10.1029/94JB01252
Christeson GL, Shaw PR, Garmany JD (1997) Shear and compressional wave structure of the east pacific rise, 9°–10°N. J Geophysical Res Solid Earth 102(B4):7821–7835. https://doi.org/10.1029/96JB03901
Christeson GL, Wilcock WSD, Purdy GM (1994) The shallow attenuation structure of the fast-spreading east pacific rise near 9°30′N. Geophys Res Lett 21(5):321–324. https://doi.org/10.1029/94GL00189
Christeson GL, Karson JA, McIntosh KD (2010) Mapping of seismic layer 2A/2B boundary above the sheeted dike unit at intermediate spreading crust exposed near the blanco transform. Geochem Geophys Geosyst. https://doi.org/10.1029/2009GC002864
Christeson GL, McIntosh KD, Karson JA (2007) Inconsistent correlation of seismic layer 2a and lava layer thickness in oceanic crust. Nature 445(7126):418–421. https://doi.org/10.1038/nature05517
Christensen NI, Shaw GH (1970) Elasticity of mafic rocks from the Mid-Atlantic Ridge. Geophys J R Astron Soc 20(3):271–284
Coleman RG (1977) Ophiolites, ancient oceanic lithosphere? Springer, New York
Collier JS, Singh SC (1998) Poisson's ratio structure of young oceanic crust. J Geophysical Res Solid Earth 103(B9):20981–20996. https://doi.org/10.1029/98JB01980
Davies JH, Bickle MJ (1991) A physical model for the volume and composition of melt produced by hydrous fluxing above subduction zones. Philosophical Transact Phys Sci Eng 335(1638):355–364
Detrick R, Collins J, Stephen R, Swift S (1994) In situ evidence for the nature of the seismic layer 2/3 boundary in oceanic crust. Nature 370(6487):288–290. https://doi.org/10.1038/370288a0
Detrick RS, Toomey DR, Collins JA (1998) Three-dimensional upper crustal heterogeneity and anisotropy around hole 504B from seismic tomography. J Geophysical Res Solid Earth 103(B12):30485–30504. https://doi.org/10.1029/98JB02409
Dilek Y, Furnes H (2011) Ophiolite genesis and global tectonics: geochemical and tectonic fingerprinting of ancient oceanic lithosphere. Geol Soc Am Bull 123(3–4):387–411. https://doi.org/10.1130/B30446.1
Dunn RA (2015) Tracking stress and hydrothermal activity along the eastern Lau spreading center using seismic anisotropy. Earth Planet Sci Lett 410(January):105–116. https://doi.org/10.1016/j.epsl.2014.11.027
Dunn RA, Martinez F (2011) Contrasting crustal production and rapid mantle transitions beneath back-arc ridges. Nature 469(7329):198–202. https://doi.org/10.1038/nature09690
Dunn RA, Martinez F, Conder JA (2013) Crustal construction and magma chamber properties along the eastern lau spreading center. Earth Planet Sci Lett 371–372(June):112–124. https://doi.org/10.1016/j.epsl.2013.04.008
Eason DE, Dunn RA (2015) Petrogenesis and structure of oceanic crust in the Lau Back-Arc Basin. Earth Planet Sci Lett 429(November):128–138. https://doi.org/10.1016/j.epsl.2015.07.065
Eccles JD, White RS, Christie PAF (2009) Identification and inversion of converted shear waves: case studies from the european north atlantic continental margins. Geophys J Int 179(1):381–400. https://doi.org/10.1111/j.1365-246X.2009.04290.x
Escrig S, Bézos A, Goldstein SL, Langmuir CH, Michael PJ (2009) Mantle source variations beneath the Eastern Lau Spreading Center and the nature of subduction components in the Lau basin–Tonga arc system. Geochem Geophys Geosyst 10:Q04014. https://doi.org/10.1029/2008GC002281
Ferrini VL, Tivey MK, Carbotte SM, Martinez F, Roman C (2008) Variable morphologic expression of volcanic, tectonic, and hydrothermal processes at six hydrothermal vent fields in the Lau Back-Arc Basin. Geochem Geophys Geosyst. https://doi.org/10.1029/2008GC002047
Gaetani GA, Grove TL (1994) Melting in the sub-arc mantle: the effects of H2O on primary magmas and the spinel-to-garnet transition. Mineral Mag 58A(1):301–302. https://doi.org/10.1180/minmag.1994.58A.1.158
Guevara SE, Stewart RR (1998) Multicomponent seismic polarization analysis. CREWES Research Report 10:7–19
Hamilton EL (1979) V_p / V_s and Poisson's ratios in marine sediments and rocks. J Acoustical Soc Am 66(4):1093–1101. https://doi.org/10.1121/1.383344
Harding AJ, Kent GM, Orcutt JA (1993) A multichannel seismic investigation of upper crustal structure at 9°N on the east pacific rise: implications for crustal accretion. J Geophysical Res Solid Earth 98(B8):13925–13944. https://doi.org/10.1029/93JB00886
Hawkins JW (1994) Petrologic synthesis: Lau Basin Sransect (Leg 135). In: Hawkins J, Parson L, Allan J (eds) Proceedings of the ocean drilling program leg 135, scientific results. Ocean drilling program. College Station, TX, pp 879–905
Hawkins JW (1995) Evolution of the Lau Basin Insights from ODP Leg 135. Brian Taylor James Natland eds Geophysical Monograph Series. American Geophysical Union Washington DC. 88:125–173.
Hirth G, Kohlstedt DL (1996) Water in the oceanic upper mantle: implications for rheology, melt extraction and the evolution of the lithosphere. Earth Planet Sci Lett 144(1–2):93–108. https://doi.org/10.1016/0012-821X(96)00154-9
Holland PW, Welsch RE (1977) Robust regression using iteratively reweighted least-squares. Communications Statistics Theory Methods 6(9):813–827. https://doi.org/10.1080/03610927708827533
Jacobs AM, Harding AJ, Kent GM (2007) Axial crustal structure of the lau back-arc basin from velocity modeling of multichannel seismic data. Earth Planet Sci Lett 259(3–4):239–255. https://doi.org/10.1016/j.epsl.2007.04.021
Jenner GA, Cawood PA, Rautenschlein M, White WM (1987) Composition of Back-Arc Basin Volcanics, Valu Fa Ridge, Lau Basin: evidence for a slab-derived component in their mantle source. J Volcanol Geoth Res 32(1):209–222. https://doi.org/10.1016/0377-0273(87)90045-X
Karig DE (1970) Ridges and basins of the tonga-kermadec island arc system. J Geophys Res 75(2):239–254. https://doi.org/10.1029/JB075i002p00239
Karson, Jeffrey A. 1998. Internal Structure of Oceanic Lithosphere A: Perspective from Tectonic Windows. W Roger Buck, Paul T Delaney, Jeffrey A Karson, and Yves Lagabrielle eds Geophysical Monograph Series. American Geophysical Union, Washington DC. 177–218
Karson JA, Klein EM, Hurst SD, Lee CE, Rivizzigno PA, Curewitz D, Morris AR et al (2002) Structure of uppermost fast-spread oceanic crust exposed at the hess deep rift: implications for

subaxial processes at the east pacific rise. Geochem Geophys Geosyst. https://doi.org/10.1029/2001GC000155
Kent AJR, Peate DW, Newman S, Stolper EM, Pearce JA (2002) Chlorine in submarine glasses from the lau basin: seawater contamination and constraints on the composition of slab-derived fluids. Earth Planet Sci Lett 202(2):361–377. https://doi.org/10.1016/S0012-821X(02)00786-0
Kenter, Jeroen A.M., and Michael Ivanov. 1995. Proceedings of the Ocean Drilling Program, 143 Scientific Results. EL Winterer WW Sager JV Firth JM Sinton. 143. Proceedings of the Ocean Drilling Program. Ocean Drilling Program. https://doi.org/10.2973/odp.proc.sr.143.1995.
Kim E, Toomey DR, Hooft EEE, Wilcock WSD, Weekly RT, Lee S-M, Kim YH (2018) Upper crustal *Vp* / *Vs* ratios at the endeavour segment, Juan de Fuca ridge, from joint inversion of *P* and *S* travel times: implications for hydrothermal circulation. Geochem Geophys Geosyst. https://doi.org/10.1029/2018GC007921
Levander AR (1988) Fourth-order finite-difference *P-SV* seismograms. Geophysics 53:1425–1436. https://doi.org/10.1190/1.1442422
Lin J, Morgan JP (1992) The spreading rate dependence of three-dimensional mid-ocean ridge gravity structure. Geophys Res Lett 19(1):13–16. https://doi.org/10.1029/91GL03041
Livermore R, Cunningham A, Vanneste L, Larter R (1997) Subduction influence on magma supply at the east scotia ridge. Earth Planet Sci Lett 150(3–4):261–275. https://doi.org/10.1016/S0012-821X(97)00074-5
Margrave GF (2000) New seismic Modelling facilities in Matlab. CREWES Research Report 12:45
Martinez F, Taylor B (2002) Mantle wedge control on back-arc crustal accretion. Nature 416(6879):417–420. https://doi.org/10.1038/416417a
Martinez F, Taylor B, Baker ET, Resing JA, Walker SL (2006) Opposing trends in crustal thickness and spreading rate along the back-arc eastern lau spreading center: implications for controls on ridge morphology, faulting, and hydrothermal activity. Earth Planet Sci Lett 245(3–4):655–672. https://doi.org/10.1016/j.epsl.2006.03.049
Michael PJ, Escrig S, Bezos A, Langmuir CH, Arculus RJ, Goddard CI (2011) Along- and across-arc basalt geochemical trends of seamounts in lau basin: evidence for fluid components and mantle melting. AGU Fall Meeting Abstracts 54(December):V54B – V62
Morgan JP, John Chen Y (1993a) The genesis of oceanic crust: magma injection, hydrothermal circulation, and crustal flow. J Geophysical Res Solid Earth 98(B4):6283–6297. https://doi.org/10.1029/92JB02650
Morgan JP, John Chen Y (1993b) Dependence of ridge-axis morphology on magma supply and spreading rate. Nature 364(6439):706–708. https://doi.org/10.1038/364706a0
Nicolas A 1989 The Various Ophiolites and Their Oceanic Environments of Origin. A Nicolas Structures of Ophiolites and Dynamics of Oceanic Lithosphere Petrology and Structural Geology. Springer Netherlands Dordrecht 187–201 https://doi.org/https://doi.org/10.1007/978-94-009-2374-4_8.
Parmentier EM, Morgan JP (1990) Spreading rate dependence of three-dimensional structure in oceanic spreading centres. Nature 348(6299):325–328. https://doi.org/10.1038/348325a0
Parson LM, Pearce JA, Murton BJ, Hodkinson RA (1990) Role of ridge jumps and ridge propagation in the tectonic evolution of the lau back-arc basin, southwest pacific. Geology 18(5):470. https://doi.org/10.1130/0091-7613(1990)018%3c0470:RORJAR%3e2.3.CO;2
Peacock SM, Christensen NI, Bostock MG, Audet P (2011) High pore pressures and porosity at 35 km depth in the cascadia subduction zone. Geology 39(5):471–474. https://doi.org/10.1130/G31649.1
Pearce JA, Ernewein M, Bloomer SH, Parson LM, Murton BJ, Johnson LE (1994) Geochemistry of Lau Basin volcanic rocks: influence of ridge segmentation and arc proximity. Geological Soc London Special Publications 81(1):53–75. https://doi.org/10.1144/GSL.SP.1994.081.01.04
Peirce C, Turner IM, Sinha MC (2001) Crustal structure, accretionary processes and rift propagation: a gravity study of the intermediate-spreading valu fa ridge, lau basin. Geophys J Int 146(1):53–73. https://doi.org/10.1046/j.0956-540x.2001.01445.x
Perfit MR 2001 Mid-Ocean Ridge Geochemistry and Petrology. Encyclopedia of Ocean Sciences 815 825. Elsevier UK https://doi.org/10.1016/B978-012374473-9.00096-5.
Reid I, Jackson HR (1981) Oceanic spreading rate and crustal thickness. Mar Geophys Res 5(2):165–172. https://doi.org/10.1007/BF00163477
Saar MO, Manga M (1999) Permeability-Porosity Relationship in Vesicular Basalts. Geophys Res Lett 26(1):111–114. https://doi.org/10.1029/1998GL900256
Shearer PM (1988) Cracked media, poisson's ratio and the structure of the upper oceanic crust. Geophys J Int 92(2):357–362. https://doi.org/10.1111/j.1365-246X.1988.tb01149.x
Sisson TW, Grove TL (1992) experimental investigations of the role of H2O in calc-alkaline differentiation and subduction zone magmatism. Contrib Miner Petrol 113(2):143–166. https://doi.org/10.1007/BF00283225
Sleeper JD, Martinez F (2014) Controls on segmentation and morphology along the back-arc eastern lau spreading Center and Valu Fa Ridge. J Geophysical Res Solid Earth 119(3):1678–1700. https://doi.org/10.1002/2013JB010545
Small C, Sandwell DT (1989) An abrupt change in ridge axis gravity with spreading rate. J Geophysical Res Solid Earth 94(B12):17383–17392. https://doi.org/10.1029/JB094iB12p17383
Spudich P, Orcutt J (1980) Petrology and porosity of an oceanic crustal site: results from wave form modeling of seismic refraction data. J Geophysical Res Solid Earth 85(B3):1409–1433. https://doi.org/10.1029/JB085iB03p01409
Stern RJ, Bloomer SH, Martinez F, Yamazaki T, Mark Harrison T (1996) The composition of back-arc basin lower crust and upper mantle in the mariana trough: a first report. Island Arc 5(3):354–372. https://doi.org/10.1111/j.1440-1738.1996.tb00036.x
Stolper E, Newman S (1994) The role of water in the petrogenesis of mariana trough magmas. Earth Planet Sci Lett 121(3):293–325. https://doi.org/10.1016/0012-821X(94)90074-4
Tamura A, Arai S, Ishimaru S, Andal ES (2008) Petrology and geochemistry of peridotites from IODP Site U1309 at Atlantis Massif, MAR 30°N: micro- and macro-scale melt penetrations into peridotites. Contrib Miner Petrol 155(4):491–509
Taylor B, Zellmer KE, Martinez F, Goodliffe A (1996) Sea-floor spreading in the Lau Back-Arc Basin. Earth Planet Sci Lett 144(1–2):35–40. https://doi.org/10.1016/0012-821X(96)00148-3
Thorbecke JW, Draganov D (2011) Finite-difference modeling experiments for seismic interferometry. Geophysics 76(6):H1-18. https://doi.org/10.1190/geo2010-0039.1
Turner IM, Peirce C, Sinha MC (1999) Seismic Imaging of the axial region of the Valu Fa ridge, Lau Basin-the accretionary processes of an intermediate back-arc spreading ridge. Geophys J Int 138(2):495–519. https://doi.org/10.1046/j.1365-246X.1999.00883.x
Vallier TL, Jenner GA, Frey FA, Gill JB, Davis AS, Volpe AM, Hawkins JW et al (1991) Subalkaline andesite from valu fa ridge, a back-arc spreading center in southern Lau Basin: petrogenesis, comparative chemistry, and tectonic implications. Chem Geol 91(3):227–256. https://doi.org/10.1016/0009-2541(91)90002-9
Vera EE, Diebold JB (1994) Seismic imaging of oceanic layer 2A between 9°30′N and 10°N on the east pacific rise from

two-ship wide-aperture profiles. J Geophysical Res Solid Earth 99(B2):3031–3041. https://doi.org/10.1029/93JB02107

White RS, Stephen RA (1980) Compressional to shear wave conversion in oceanic crust. Geophys J Int 63(2):547–565. https://doi.org/10.1111/j.1365-246X.1980.tb02637.x

White RS, McKenzie D, Keith O'Nions R (1992) Oceanic crustal thickness from seismic measurements and rare earth element inversions. J Geophysical Res Solid Earth 97(B13):19683–19715. https://doi.org/10.1029/92JB01749

Wiedicke M, Collier J (1993) Morphology of the Valu Fa spreading ridge in the southern Lau Basin. J Geophysical Res Solid Earth 98(B7):11769–11782. https://doi.org/10.1029/93JB00708

Wilcock WSD, Solomon SC, Purdy GM, Toomey DR (1995) Seismic attenuation structure of the east pacific rise near 9°30′N. J Geophysical Res Solid Earth 100(B12):24147–24165. https://doi.org/10.1029/95JB02280

Wilkens RH, Fryer GJ, Karsten J (1991) Evolution of porosity and seismic structure of upper oceanic crust: importance of aspect ratios. J Geophysical Res Solid Earth 96(B11):17981–17995. https://doi.org/10.1029/91JB01454

Zellmer KE, Taylor B (2001) A Three-Plate Kinematic Model for Lau Basin Opening. Geochem Geophys Geosyst. https://doi.org/10.1029/2000GC000106

Zoeppritz K (1919) On the reflection and propagation of seismic waves. Gottinger Nachrichten, I, 66–84